PERSPECTIVE

Check for updates

All publication charges for this article have been paid for by the Royal Society of Chemistry

Layered transition metal oxides (LTMO) for oxygen evolution reactions and aqueous Li-ion batteries

Yohan Kim, [iD] Eunjin Choi, [iD] Seunggu Kim [iD] and Hye Ryung Byon [iD] *

This perspective paper comprehensively explores recent electrochemical studies on layered transition metal oxides (LTMO) in aqueous media and specifically encompasses two topics: catalysis of the oxygen evolution reaction (OER) and cathodes of aqueous lithium-ion batteries (LiBs). They involve conflicting requirements; OER catalysts aim to facilitate water dissociation, while for cathodes in aqueous LiBs it is essential to suppress water dissociation. The interfacial reactions taking place at the LTMO in these two distinct systems are of particular significance. We show various strategies for designing LTMO materials for each desired aim based on an in-depth understanding of electrochemical interfacial reactions. This paper sheds light on how regulating the LTMO interface can contribute to efficient water splitting and economical energy storage, all with a single material.

1. Introduction

Electrochemical conversion and storage systems are currently receiving significant attention for utilizing green and sustainable energy sources. Carbon dioxide emissions from fossil fuels are the primary driver of the climate crisis. Thus, it is imperative for society to shift towards alternative and clean energy sources while also developing effective means of storing them as electrical energy.

Among the promising energy sources, hydrogen (H_2) stands out prominently.[1,2] Extensive research efforts have been dedicated to exploring green H_2 production through electrochemical water splitting. However, the water-splitting process faces a significant hurdle in the form of the sluggish oxygen evolution reaction (OER), which acts as the counter-reaction to hydrogen production in electrolyzers.[3,4] Consequently, the development of efficient OER catalysts becomes a critical undertaking in realizing the vision of efficient and sustainable green H_2 production.

Meanwhile, rechargeable batteries are quintessential energy storage systems, offering unparalleled capabilities in storing and releasing energy. At the heart of these batteries lies the lithium-ion (Li^+).[5,6] This charge carrier with light weight and high electrochemical reduction potential holds promise for achieving high energy density. In order to maximize energy density, it becomes critical to develop electrodes that can accommodate a greater influx of Li^+ ions alongside the flow of electrons. Layered, spinel, and olivine structures have emerged as notable electrodes.[7,8] Among them, layered oxides provide

superior capacity and stable cyclability, thus being investigated considerably for achieving high energy density.[9,10] In particular, lithium cobalt oxide $LiCoO_2$ (referred to as LCO) and lithium nickel cobalt manganese oxide ($LiNi_xCo_yMn_zO_2$, $x + y + z = 1$, denoted as NCM) as members of layered transition metal oxide (LTMO) are commercially successful cathodes of LiBs. Further, beyond their utilization in non-aqueous media, new research approaches have recently been explored in aqueous media. Aqueous lithium-ion batteries (LiBs) are cheaper and have a low fire risk, making them suitable for grid-scale energy storage systems (ESSs) linked to sustainable energy devices.[11]

These demands and scientific curiosity have spurred numerous material studies for OER catalysts and cathodes of aqueous LiBs. In particular, LTMO shows intriguing characteristics when applied for both purposes. The LTMO is vulnerable and prone to deformation in water. However, the resulting surface or bulk structural transformations can manifest OER activity. For example, after Li^+ extraction from LCO, the oxidized transition metals facilitate the OER.[12] Continuous Li^+ removal further activates the oxide (consisting of O^{2-} anions) of LCO by tuning the electronic structure, eventually providing multiple OER active sites. Importantly, these enriched parameters are attractive to understanding the origin of OER active sites and rendering better activity. As a cathode in aqueous LiBs, LTMO is seemingly undesired due to extreme water sensitivity and the corresponding structural distortion. In particular, protons (H^+) are inserted into LTMO during the charging and discharging process which significantly exacerbates structural degradation and cell failure.[13] Therefore, regulating electrochemical interfacial reactions for selective Li^+ inflow while preventing H^+ access is essential to protect LTMO structures in aqueous LiBs.

Interestingly, two vital applications require conflicting properties for LTMO, which presents a challenge.[4,14-17] An

Department of Chemistry, Korea Advanced Institute of Science and Technology (KAIST), 291, Daehak-ro, Yuseong-gu, Daejeon 34141, Republic of Korea. E-mail: hrbyon@kaist.ac.kr

efficient OER catalyst necessitates a high affinity and fast adsorption of OH$^-$ to facilitate oxidation to O$_2$, while reversible Li$^+$ storage requires minimizing the incorporation of water molecules to prevent irreversible H$^+$ insertion. Addressing these contradicting demands calls for novel approaches that involve a profound understanding of the interfacial regions through a combination of *in situ/ex situ* electrochemical analyses and computational simulations. This approach enables a comprehensive examination of electrochemical reactions and facilitates the design of LTMO materials tailored to specific electrochemical conditions.[18,19]

In the following sections, we discuss these different purposes separately and the versatile tuning of LMTO according to the target aims. The crystal and electronic structure background of LTMO is introduced in Section 2. In Section 3, we present various strategies for designing OER catalysts through structural modifications of LTMO. Section 4 focuses on the origin of cathode degradation in aqueous LiBs. In addition, we introduce various *in situ/ex situ* observations and computational simulations to provide insight into the interfacial reactions where Li$^+$ intercalation competes with H$^+$ insertion.

2. Layered transition metal oxide (LTMO)

The development of LTMO reached significant milestones after demonstrating LCO with the reversible extraction and incorporation of Li$^+$ ions. This breakthrough led to the successful implementation of LCO as the cathode in conjunction with a graphite anode, giving rise to the first commercially viable LiBs in 1991.[20]

Structurally, LTMO consists of an alternating alkali metal ion layer and transition metal (M) oxide layer, denoted as MO$_2$, and crystallizes in the $R\bar{3}m$ (no. 166) space group[21] (Fig. 1(a)). The MO$_2$ layers consist of edge-sharing MO$_6$ octahedral units. Within the layered arrangement, alkali metal ions are coordinated with the oxygen lattice in the MO$_2$ layer, adopting octahedral, tetrahedral, or prismatic configurations. The oxygen atoms can also occupy three possible sites on a hexagonal lattice. For example, LCO adopts an O3-type structure, indicating octahedral (O) oxygen coordination for Li$^+$ and three (3) transition metal layers in the stacking unit.[9,22–24]

For electrochemistry, an oxidation process (*i.e.*, an anodic reaction) enables the extraction of Li$^+$, which is indicated as delithiation, Li$^+$ deintercalation, or Li$^+$ deinsertion. This process increases the valence state ($n+$) of the M^{n+} to balance the overall charge (eqn (1)).[24] For instance, during the charging process, LCO undergoes delithiation, accompanied by the oxidation of Co^{3+} to Co^{4+} at approximately 4.0 V *vs.* Li/Li$^+$ (equivalent to 0.96 V *vs.* SHE). The amount of extracted Li$^+$ is restricted to 50% of the total Li$^+$ quantity for LCO when the hexagonal O3 phase is transformed to the monoclinic O1 phase,[12,25] and the Co ions exist in a mixed valence state, Co^{3+}/Co^{4+}. Further extensive delithiation ($x > 0.5$ in eqn (1)) triggers an irreversible phase transition, which is undesired.[26,27] Conversely, the reverse reduction (*i.e.*, cathodic) reaction occurs
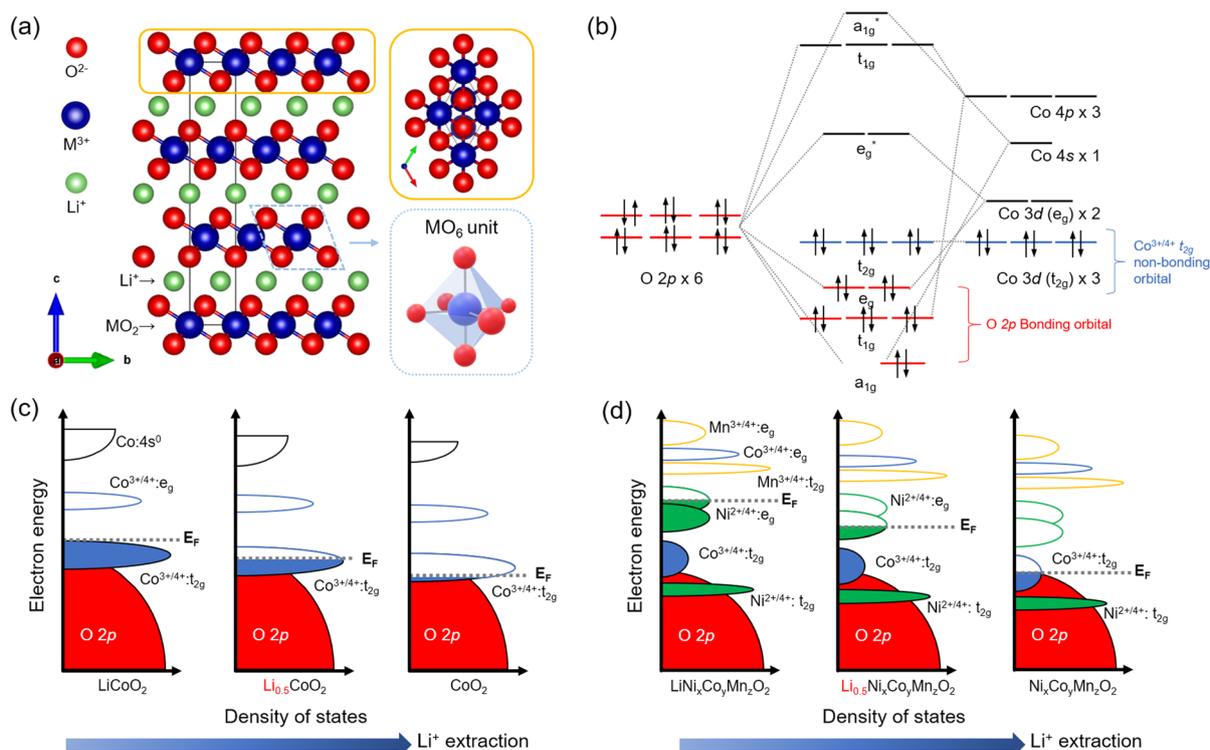

Fig. 1 Crystal and electronic structures of LTMO. (a) $R\bar{3}m$ layered LTMO. (b) Molecular orbital hybridization of an MO$_6$ octahedral unit in LiCoO$_2$ (LCO). (c and d) Electronic band structures of (c) LCO and (d) LiNi$_x$Co$_y$Mn$_z$O$_2$ ($x + y + z = 1$, NCM) by Li$^+$ extraction.

during discharge, and Li⁺ incorporation, indicated as Li⁺ intercalation, Li⁺ lithiation, or Li⁺ insertion, restores LCO to its original state. As another LTMO, NCMs involve redox events of Ni^{2+}/Ni^{4+} along with Co^{3+}/Co^{4+}, contributing to higher capacity electrodes in LiBs.

$$LiM^{n+}O_2 \rightleftharpoons Li_{1-x}M^{n+}_{1-x}M^{(n+1)+}_xO_2 + xLi^+ + xe^- \quad (1)$$
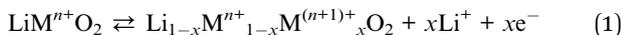
Understanding the electronic structure of LTMO is pivotal for designing electrochemical and interfacial properties during the charging and discharging process. Considering the minimal unit of an MO_6 octahedral structure, the O 2p orbitals are fully occupied by electrons in the O 2p–M nd hybridization in the molecular orbital diagram (where n is the principal quantum number of d-orbital, typically 3 for d-block elements), indicating a bonding character (Fig. 1(b)). On the other hand, because of the higher energy level of the M 3d orbital than O 2p, the occupancy of t_{2g} and e_g orbitals exclusively depends on the valence states of M^{n+}. The redox events occur primarily in these t_{2g} and e_g orbitals, underpinning the close association between Li⁺ deintercalation/intercalation and the nature of the M 3d orbitals.[28]

The molecular orbital concept extends to band theory when bulk LTMO crystals composed of arrays of edge-sharing MO_6 units are considered. In the band diagram, the O 2p band, located at a low energy level, is fully filled, while the t_{2g} and e_g bands originating from the M character are positioned at higher energy levels (Fig. 1(c)). The crucial aspect is the comparison between the position of the Fermi level (E_F) and the upper boundary level of the electron-filled state (i.e., valence band). During the anodic (delithiation) processes, the depletion of electrons from the t_{2g} bands leads to a downward shift of E_F. In the case of LCO, where 50% of the total Li⁺ is extracted, E_F is lowered towards the t_{2g} band.[9] Continued oxidation drives E_F to lower energy levels, eventually reaching the O 2p band. The E_F lying in the O 2p band activates the oxygen lattice in LCO to participate in the redox process. However, severe activation compromises the structural stability of the material and exacerbates irreversible phase transitions.[26,27]

In the band diagram for NCM, both Ni^{2+} and Co^{3+} are involved in the redox reaction. Ni^{2+}/Ni^{4+} undergoes a two-electron transfer process in the e_g band, while Co^{3+}/Co^{4+} participates in a one-electron transfer process in the t_{2g} band (Fig. 1(d)). The Mn^{4+}/Mn^{5+} band, located at a lower energy level, is fully occupied with electrons and remains inactive during the charging and discharging processes. Severe delithiation induces cation mixing, with M^{n+} occupying the Li vacancy sites and causing deformation of the layered structure to spinel (space group $Fd\bar{3}m$ (no. 227)) or rock-salt phases (space group $Fm\bar{3}m$ (no. 225)).[29] This structural transformation is particularly prominent at the surface and is more serious at higher Ni ion contents due to the instability of phases derived from Ni^{3+}.[30]

The deformation of LTMO in LiBs has traditionally been considered undesirable due to irreversible and unstable electrochemical reactions. However, recent studies have explored structure designs of LTMO by deformation to gain insights into new interfacial reactions. In aqueous electrolyte solutions, harsh anodic reactions not only facilitate the extraction of the original alkali metal ions (e.g., Li⁺) but also allow the insertion of foreign cations, including H⁺, into the Li vacancy sites. Activating the oxide under stringent conditions leads to the participation of the oxygen lattice in the electrode reaction. These approaches have deepened our understanding of the characteristics of LTMO and broadened the scope of applications.

3. LTMO as an electrocatalyst for oxygen evolution

The OER from an aqueous electrolyte solution has been developed as the counterpart reaction of green-fuel processes such as hydrogen evolution (HER), carbon dioxide reduction, and nitrate reduction. The OER has gained wide utilization due to the availability of simple and low-cost anodic processes that can be coupled with green fuel in the aqueous electrolyte solution. However, the sluggish nature of the OER governs the overall kinetics in green-fuel electrochemistry. For instance, in the production of green hydrogen through water splitting, one H_2 molecule is formed via a two-electron transfer reduction. In

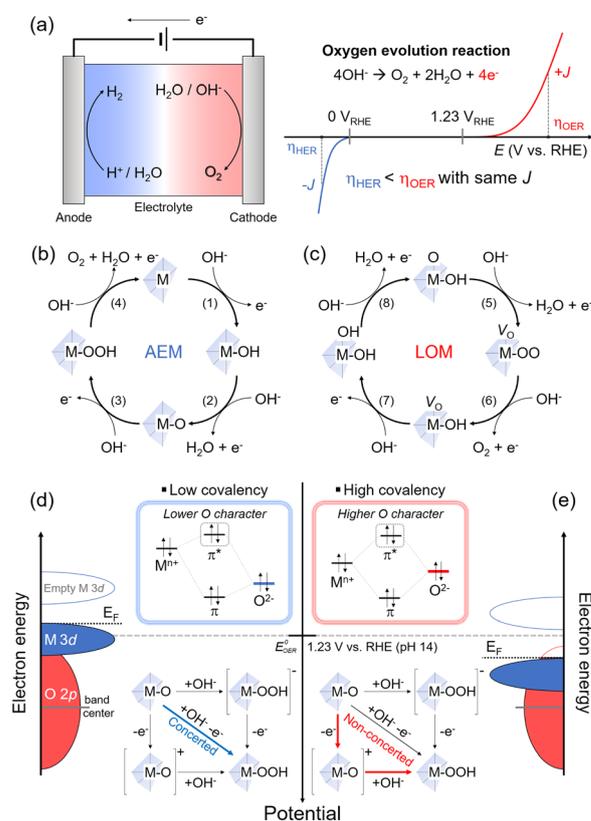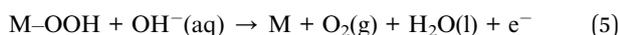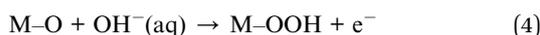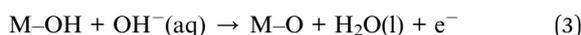**Fig. 2** Two principal OER processes. (a) Schematic illustration of the water splitting cell and I–V curve for the HER and OER. Mechanism scheme of the 4-electron transferring oxygen evolution reaction by (b) the adsorbate evolution mechanism (AEM) and (c) lattice oxygen mediated (LOM) pathway. Schematic band diagram of (d) low covalent and (e) high covalent transition metal oxides. The concerted and non-concerted one-electron transfer processes are illustrated, respectively.

comparison, the OER process involves a four-electron transfer for the evolution of one O_2 molecule (Fig. 2(a)). These multiple electron-transfer processes in the OER limit the overall efficiency of the process.[31,32] Therefore, electrocatalysts are necessary to improve the OER kinetics. While RuO_x and IrO_x are known to be efficient OER catalysts, their high costs make them impractical for widespread use. Alternatively, various transition metal oxides, including LTMO (*e.g.*, Li_xCoO_2 and Na_xCoO_2 ($0 < x < 1$)),[33–36] spinel, and perovskite structures, have been developed and utilized as OER catalysts. These cost-effective catalysts can be tailored through alkali metal ion extraction,[12] element doping,[37] and surface reconstruction.[34] Although we focus on the LTMO catalyst for the OER in this perspective (Section 3.3), the fundamental mechanisms and descriptors of the OER are first introduced in Sections 3.1 and 3.2, and are applied for all transition metal oxide catalysts in the OER.
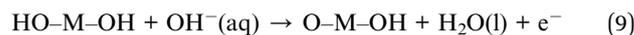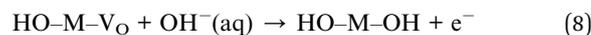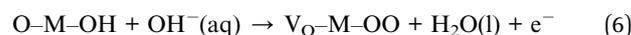
3.1. OER processes: adsorbate evolution *vs.* lattice oxygen-mediated mechanisms

Alkaline electrolyte solutions, which are enriched in hydroxide ions (OH^-), have been extensively utilized for the OER due to the instability of most transition metal oxide catalysts in acidic conditions and the slower electrochemical kinetics in neutral conditions. In alkaline environments, the OER occurs through four steps involving OH^- adsorption and electron transfer processes, as depicted in eqn (2)–(5)[3,38,39] (Fig. 2(b)). Provided that the oxide surface of transition metal oxide catalysts is very stable and inert during the OER, we only consider the adsorption of OH^- (or H_2O) above M of the catalysts as a key descriptor. Following electron transfer is faster than the adsorption as typically accompanied by the proton coupling process.[3,38] Thus, the M^{n+} acts as the active site, where OH^- is bound *via* the one-electron transfer (eqn (2)). The subsequent OH^- adsorption steps and proton-coupled electron transfer form M–O with H_2O leaving, followed by formation of M–OOH as the intermediate (eqn (3) and (4)), and the last step evolves O_2 gas with H_2O leaving (eqn (5)). This process was indicated to follow the 'adsorbate-evolution mechanism' (AEM). The activity of OER catalysts is typically predicted from the free energy difference between M–OH and M–O intermediates (eqn (2) and (3)) in density functional theory (DFT) calculations and showed a scaling relationship with different catalytic materials and intermediates.[38]

$$M + OH^-(aq) \rightarrow M–OH + e^- \quad (2)$$

$$M–OH + OH^-(aq) \rightarrow M–O + H_2O(l) + e^- \quad (3)$$

$$M–O + OH^-(aq) \rightarrow M–OOH + e^- \quad (4)$$

$$M–OOH + OH^-(aq) \rightarrow M + O_2(g) + H_2O(l) + e^- \quad (5)$$

Unlike the assumption of the AEM for the ideal catalyst structures, practical transition metal oxide structures are imperfect and have many defects in the as-prepared states and during OER processes. These crystal defects in oxide[40–43] play a significant role as the active sites and in surface

reconstruction[34,36,44] during the OER also change the activity. This suggests that the oxide is also involved in OER activity and has developed an alternative mechanism. As the transition metal oxide surface comprises O–M–OH in the alkaline solution, the first electron transfer and OH^- adsorption form O–M–O and H_2O. Concurrently, the lattice oxygen of the oxide diffuses to the deprotonated oxide to participate in O–O coupling, while leaving behind the oxygen vacancy, denoted as V_O. Thus, the oxide surface becomes V_O–M–OO (eqn (6)). The subsequent electron-transfer process produces O_2 gas through the removal of the O–O lattice, called 'lattice oxygen redox activation (O^{2-}/O_2)'. The catalyst surface retains HO–M–V_O by adsorption of OH^- (eqn (7)). The vacancy is then filled with another OH^- and electron transfer, resulting in HO–M–OH (eqn (8)). The subsequent deprotonation with the fourth electron transfer recovers the catalyst to the original form (eqn (9)). A substantial difference from the AEM is the participation of lattice oxygen in the OER and the formation of a V_O intermediate. This process is indicated to follow the 'lattice oxygen-mediated mechanism' (LOM), and the above processes are summarized in the following four consecutive equations.[4,45,46] (Fig. 2(c))

$$O–M–OH + OH^-(aq) \rightarrow V_O–M–OO + H_2O(l) + e^- \quad (6)$$

$$V_O–M–OO + OH^-(aq) \rightarrow HO–M–V_O + O_2(g) + e^- \quad (7)$$

$$HO–M–V_O + OH^-(aq) \rightarrow HO–M–OH + e^- \quad (8)$$

$$HO–M–OH + OH^-(aq) \rightarrow O–M–OH + H_2O(l) + e^- \quad (9)$$

For the LOM, the lattice oxygens (in other words, oxygen ligands for M^{n+}) should be activated, and this activation is determined from the E_F position lying in the O 2p band. Namely, as the oxidation lowers E_F, a part of the O 2p band below the E_F initiates the ligand oxygen redox activation.[46] This concept is applied for catalyst designs to modulate electronic structure. For example, the O 2p band upshifts close to E_F by lattice distortion,[41,47] or the transition metal d band and E_F downshift using the high valence state of transition metals.[48,49] These approaches cause a significant band overlap between the M 3d and the O 2p (without considerable extraction of alkali metal ions in the case of LTMO) and enhance the hybridization between M^{n+} and the oxygen ligand, indicating strong 'covalency' of the M^{n+}–O bond.

The concept of covalency is developed to explain the enhanced OER kinetics based on the oxide surface. It refers to hybridized orbitals that mix the M 3d t_{2g} and O 2p molecular orbitals. A large energy gap between M and O orbitals leads to shallow hybridization and causes low covalency (Fig. 2(d)). This indicates more ionic property in the orbital and low O character in π^* orbitals in hybridization. A typical transition metal oxide catalyst shows low covalency and stronger ionic character. In addition, as the E_F and the thermodynamic OER potential (E_{OER}^o) are close to the occupied M 3d t_{2g} band, the M^{n+} character determines the catalyst property. However, hybridized orbitals are altered when the M 3d t_{2g} band moves

downward and close to the O 2p band; when the M 3d t_{2g} orbitals overlap with the O 2p deeply, the covalency becomes stronger (Fig. 2(e)). The π* orbitals have a strong O character in the hybridization, thus making the oxygen lattice participate in the redox reaction. The LOM is predominant as the E_F lies in the O 2p band and is lower than E_{OER}^o while the electronic conductivity is high.

When the E_F is located below E_{OER}^o, the surface charge is built in equilibrium with the electrolyte solution. The negative charges, *e.g.*, electron (from the electrode) and OH⁻ (from the electrolyte solution), are accumulated at the metal oxide catalyst surface. In the presence of the highly electronic conductive catalysts (*e.g.*, semi-metal or metal), the OH⁻ adsorption rate becomes the rate-determining step due to deprotonation or acid–base pre-equilibrium process[4] (Fig. 2(e)). However, this OH⁻ adsorption process becomes faster with increasing OH⁻ concentrations at high pH.[46,50] Thus, the LOM is highly sensitive to the solution pH; low OH⁻ concentrations at lower pH limit the OER kinetics relative to the electron transfer in the electronically conductive catalyst.[14]

The above two mechanisms, AEM and LOM, rely on different key factors determining OER activity and guiding the design of OER catalysts. Conversely, the OER process of new catalysts can be addressed by the valence state (n+) of M^{n+}, pH-dependent OER activity, isotopic labeling of oxygen in catalysts or

water,[46] oxygen stoichiometry of catalysts,[48,50] structural defects of catalysts,[41,48] and so on.

3.2. Descriptors of OER activity

Identifying OER descriptors is pivotal to predicting the activity trend and guiding catalyst design principles. Here we introduce four descriptors of transition metal oxide catalysts.

3.2.1 d-Orbital structure of the metal centre (M^{n+}). The electron occupancy in the anti-bonding e_g orbital is the critical descriptor for the OER, demonstrated by perovskite and spinel oxide catalysts.[31,51–53] As more electrons occupy the e_g orbital by increased d-electron number of M^{n+}, the anti-bonding character in the M–O bond is enhanced while the binding strength of the OER intermediates weakens.[54] Shao-Horn and coworkers investigated the correlation between the e_g orbital occupancy and the adsorption of OER intermediates and demonstrated the improved OER kinetics when the average e_g occupancy approaches near unity in perovskite materials[31] (Fig. 3(a)).

The valence and spin states of M^{n+} in the d orbital also determine M and oxygen ligand interactions. Another important aspect is the valence state (n+) of M^{n+}. The OER activity is typically better with higher valence states of M. The delithiated LCO ($Li_{0.5}CoO_2$), where Co^{3+} and Co^{4+} co-exist, improves electrophilicity, electrical conductivity, Co–O bond covalency, and OH⁻ binding affinity compared to the pristine LCO where Co^{3+}
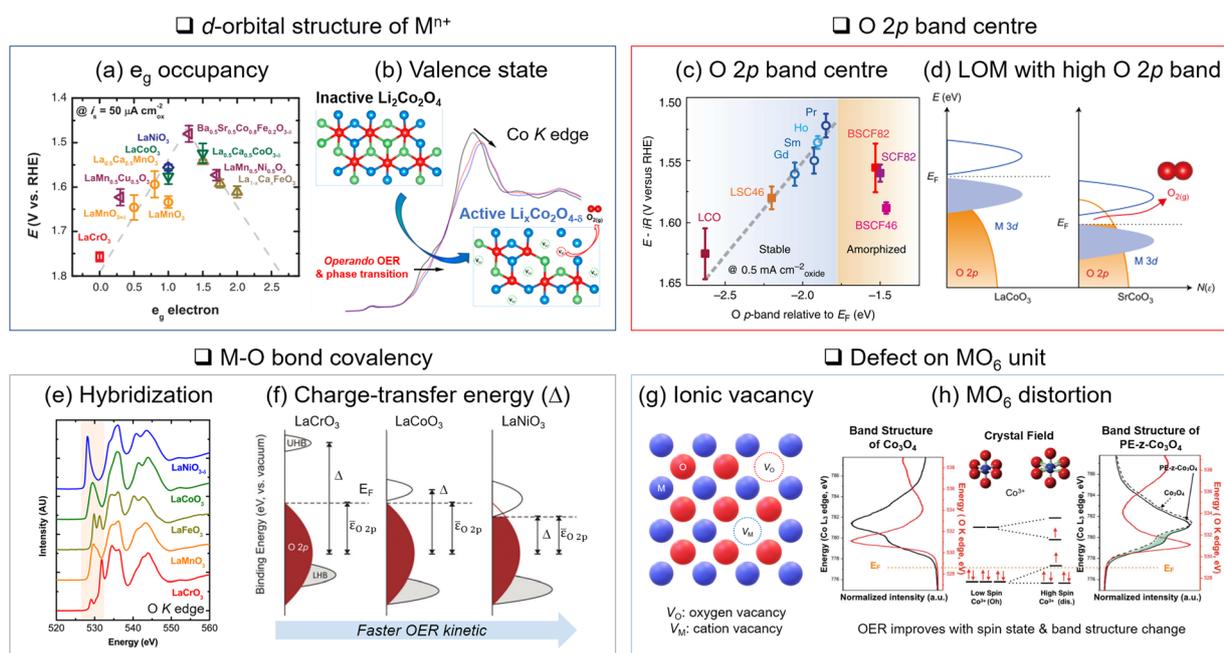
Fig. 3 Descriptors of OER activity. (a) Relationship between e_g occupancy and OER activity for perovskite oxide. Adapted with permission from ref. 31. Copyright 2011 The American Association for the Advancement of Science. (b) *In situ* monitoring of valence state change through X-ray absorption spectroscopy and active phase generation on $Li_2Co_2O_4$. Adapted with permission from ref. 57. Copyright 2019 American Chemical Society. (c) Higher OER activity with a closer O 2p band centre position to the Fermi level (E_F). Adapted with permission from ref. 72. Copyright 2013 Springer Nature. (d) Lattice oxygen mediated (LOM) OER activated by the E_F position in the O 2p band. Adapted with permission from ref. 46. Copyright 2017 Springer Nature. (e) Estimation of metal–oxygen bond hybridization with O K-edge X-ray absorption. Adapted with permission from ref. 80. Copyright 2014 American Chemical Society. (f) Relationship between covalency and charger transfer energy enhancing OER activity. Adapted with permission from ref. 14. Copyright 2017 Royal Society of Chemistry. (g) Schematic illustration of ionic vacancy. (h) MO_6 distortion and corresponding changes in molecular orbital and electronic band structure. Adapted with permission from ref. 87. Copyright 2018 John Wiley and Sons.

only exists.[12] This is attributed to the downshift of the d band and E_F level with the increasing valence state of Co. The lowered d band can be overlapped with the O 2p band and enhances the Co–O covalency. In addition, the lowered E_F activates the lattice oxygen.[49] Thus, the higher valence state of M^{n+} increases OER activity *via* the LOM.

The valence state can also be tuned by cation doping[48] or anodic potential increase.[49,55,56] The extraction of Li^+ or Na^+ from LTMO is a good example, where the valence state of M is increased.[57–59] Zhang and coworkers reported that spontaneous delithiation on spinel $Li_2Co_2O_4$ oxidized Co^{3+} to Co^{4+} below or at OER potentials and created an OER active surface[57] (Fig. 3(b)).

To observe the alternation of the valence state of M^{n+} during the OER, *in situ*/*operando* X-ray absorption near edge structure (XANES) spectroscopy is a suitable tool.[60] In addition, extended X-ray absorption fine structure (EXAFS) spectroscopy also identifies the local structures of catalysts, including the neighbor atom distance and the coordination numbers, which are sensitively changed under the OER conditions. Thus, these X-ray absorption spectroscopies have been widely utilized to address the d-orbital structures.

3.2.2 O 2p band centre. Along with the d orbital of M^{n+},[31,72] the O 2p band structure should also be considered as the descriptor of OER activity.[73,74] The degree of electron delocalization over the oxide is critical and determined by the E_F position; the position of the O 2p band 'centre' relative to that of the E_F affects the electronic structure, the surface-oxygen exchange rate, the formation energy of oxygen vacancies, and the vacancy concentrations.[72,75,76] Grimaud and coworkers modulated the O 2p band position in Co-based double perovskite oxide[72] (Fig. 3(c)). The uplift of the O 2p band centre typically formed the stronger Co–O covalency and facilitated the OER. However, if the O 2p band centre was very close to the E_F, the oxide of the catalysts formed many oxygen vacancies and became an amorphous structure, which caused a diminishing OER activity and stability.[77] Thus, the position of the O 2p band centre relative to the E_F should be optimized[46] (Fig. 3(d)).

3.2.3 Covalency of the metal–oxygen bond. The orbital hybridization between M 3d and O 2p orbitals produces the covalent bond. This covalency concept is applied to the M–O bond character beyond the simple ionic model and is considered the critical OER descriptor. The electronic band structures control the M–O covalency, and the greater M–O covalency typically facilitates the OER rate. To enhance band hybridization, the valence state of M^{n+} can be increased[78] or dopants with high electronegativity are added for downshifting the M d-band.[79] However, the strong hybridization also leads to the formation of many oxygen vacancies[28] and reduces the electron transfer barriers.[14,32]

XANES in O K-edge reveals the electron transition from the O 1s to the M 3d–O 2p hybridized band and addresses the M–O bonding character. Shao-Horn and coworkers identified the origin of the OER activities of metal oxide catalysts, attributing them to their different covalency, although they have the same e_g occupancy based on XANES[80] (Fig. 3(e)). The energy gap between the unoccupied M 3d–O 2p band centre and the occupied O 2p band centre is also estimated to be the charge

transfer energy.[14] The partial density of states for each M 3d–O 2p and O 2p band was obtained by O Kα X-ray emission and O K-edge X-ray absorption, respectively. The smaller charge transfer energy indicates stronger covalency and improves OER kinetics (Fig. 3(f)).

3.2.4 Crystal defect. The faults of crystal structures often act as active sites and increase OER activity. The oxygen vacancy, V_O, is the representative anionic defect affecting the OER in the transition metal oxide catalysts (Fig. 3(g)). The desired V_O is thermodynamically stable and generated through low-valent cation doping,[48] thermal heating,[43] or plasma treatment.[81] By forming the V_O, the M^{n+} is surrounded by the electron-deficient oxide and acts as the OH^- adsorption site.[43,81] Breaking the six-coordinated MO_6 octahedral unit also alters the M d-orbital configuration and spin state.[82] In addition, the M–O covalency becomes stronger in the presence of V_O.[48] Similarly, cationic M^{n+} vacancies can also serve as the OER active sites by modulating the electronic structure,[83,84] water adsorbing site,[83] and intermediate stabilization.[85] Importantly, because numerous ionic vacancies weaken the catalyst stability, the vacancy concentrations should be optimized.[39,86]

Distortion of the MO_6 unit is also critical. Distortion defects are generally formed by lattice mismatches on grain boundaries,[41] lattice expansion/compression,[40,47,87,88] and A-site cation vacancies on perovskite.[42] The distortion of the octahedral structure engenders the d-orbital splitting according to ligand field theory. It changes the spin state and band structure to expedite the charge transfer to the OER intermediates. For instance, the surface lattice expansion of Co_3O_4 induced a high spin state Co^{3+} ($t_{2g}^4 e_g^2$) and increased e_g occupancy, which optimized the binding strength of intermediates to the catalyst surface[87] (Fig. 3(h)).

3.3. Applications of LTMO as an OER electrocatalyst

This section focuses on the LTMO structure and various LTMO designs to improve OER activity. The representative LTMO examples are LCO and $NaCoO_2$. Shao-Horn and coworkers investigated the OER of LCO in different pH electrolyte solutions[89] (Fig. 4). Using cyclic voltammetry (CV), the Li^+ extraction
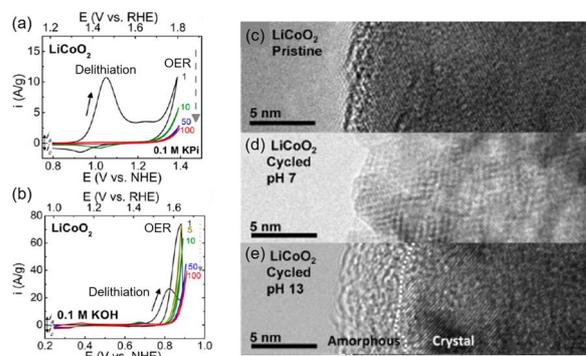

Fig. 4 Cyclic voltammogram (CV) of $LiCoO_2$ (LCO) in (a) neutral and (b) alkaline electrolytes. (c–e) TEM image of LCO (c) pristine, (d) after cycling at pH 7, and (e) after cycling at pH 13. Adapted with permission from ref. 89. Copyright 2012 American Chemical Society.

Table 1 Summary of LTMO catalytic activity and stability for the OER

Electrocatalyst	Overpotential (mV)/J^a	Tafel slope (mV dec^{-1})	Stability^b	Electrolyte	Substrate	Ref.
LiCoO$_2$	440/10 mA cm$_{geo}^{-2}$	98	—	0.1 M KOH	Glassy carbon	47
LiCoO$_2$	430/10 mA cm$_{geo}^{-2}$	89	—	0.1 M KOH	Glassy carbon	37
LiCoO$_2$	360/0.1 mA cm$_{geo}^{-2}$	48	—	0.1 M KOH	Carbon paper	12
De-LiCoO$_2$	295/0.1 mA cm$_{geo}^{-2}$	50	1000 cycles	0.1 M KOH	Carbon paper	12
LiCo$_{0.33}$Ni$_{0.33}$Fe$_{0.33}$O$_2$	320/0.1 mA cm$_{geo}^{-2}$	45	—	0.1 M KOH	Carbon paper	12
De-LiCo$_{0.33}$Ni$_{0.33}$Fe$_{0.33}$O$_2$	240/0.1 mA cm$_{geo}^{-2}$	35	1000 cycles	0.1 M KOH	Carbon paper	12
NaCoO$_2$	388/10 mA cm$_{geo}^{-2}$	51	—	1 M NaOH	Glassy carbon	61
NaCoO$_2$	380/10 mA cm$_{geo}^{-2}$	113.4	—	1 M KOH	Carbon paper	62
Na$_{0.67}$CoO$_2$	290/10 mA cm$_{geo}^{-2}$	39	5.56 h @ 1.6 V vs. RHE	0.1 M KOH	Glassy carbon	33
Na$_{0.75}$CoO$_2$	370/10 mA cm$_{geo}^{-2}$	49	5000 cycles	1 M NaOH	Glassy carbon	61
Na$_{0.6}$CoO$_2$	392/10 mA cm$_{geo}^{-2}$	53	—	1 M NaOH	Glassy carbon	63
Mg-doped LCO-NS	329/10 mA cm$_{geo}^{-2}$	33.8	—	1 M KOH	Glassy carbon	64
LiCo$_{0.8}$Fe$_{0.2}$O$_2$	350/10 mA cm$_{geo}^{-2}$	50	5 h @ 10 mA cm$_{geo}^{-2}$	0.1 M KOH	Glassy carbon	37
Na$_{0.86}$Co$_{0.95}$Fe$_{0.05}$O$_2$	450/10 mA cm$_{geo}^{-2}$	60	3 h @ 5 mA cm$_{geo}^{-2}$	0.1 M KOH	Glassy carbon	65
Na$_{0.67}$Mn$_{0.5}$Co$_{0.3}$Fe$_{0.2}$O$_2$	390/10 mA cm$_{geo}^{-2}$	67	2 h @ 5 mA cm$_{geo}^{-2}$	0.1 M KOH	Glassy carbon	66
Ag-doped Na$_{0.7}$CoO$_2$	236/10 mA cm$_{geo}^{-2}$	48	30 h @ 1.522 V vs. RHE	1 M KOH	Carbon paper	62
1% La-doped LCO	330/10 mA cm$_{geo}^{-2}$	48	10 h @ 10 mA cm$_{geo}^{-2}$	0.1 M KOH	Glassy carbon	47
LCO-NS	410/10 mA cm$_{geo}^{-2}$	88	6 h @ 1.7 V vs. RHE	0.1 M KOH	Glassy carbon	67
AD-LCO	184/10 mA cm$_{geo}^{-2}$	35.4	200 h @ 50 mA cm$_{geo}^{-2}$	1 M KOH	Glassy carbon	68
LCO-NS/NS	289/10 mA cm$_{geo}^{-2}$	75.8	20 h @ 1.52 V vs. RHE	1 M KOH	Carbon cloth	69
Pt-LCO-NS	285/10 mA cm$_{geo}^{-2}$	46.8	20 h @ 10 mA cm$_{geo}^{-2}$	1 M KOH	Glassy carbon	70
Cs$^+$-inserted LCO	392/10 mA cm$_{geo}^{-2}$	47.1	8 h @ 10 mA cm$_{geo}^{-2}$	0.1 M CsOH	Glassy carbon	36
K$^+$-inserted LCO	416/10 mA cm$_{geo}^{-2}$	60.0	2 h @ 10 mA cm$_{geo}^{-2}$	0.1 M KOH	Glassy carbon	36
α-Li$_2$IrO$_3$	290/10 mA cm$_{ox}^{-2}$	50	40 h @ 10 mA cm$_{ox}^{-2}$	0.1 M KOH	Glassy carbon	71
LiCoO$_{1.8}$Cl$_{0.2}$	270/10 mA cm$_{geo}^{-2}$	55.4	500 h @ 20 mA cm$_{geo}^{-2}$	1 M KOH	Glassy carbon	34
Co$_3$O$_4$	460/10 mA cm$_{geo}^{-2}$	76	—	1 M KOH	Glassy carbon	33
IrO$_2$	408/10 mA cm$_{geo}^{-2}$	109.3	—	1 M KOH	Glassy carbon	68
IrO$_2$	450/10 mA cm$_{geo}^{-2}$	83	5 h @ 10 mA cm$_{geo}^{-2}$	0.1 M KOH	Glassy carbon	37
IrO$_2$	310/10 mA cm$_{geo}^{-2}$	57	—	1 M KOH	Glassy carbon	33

^{a} J: current density at the overpotential. 'geo' = current normalization with the geometrical surface area of the substrate. 'ox' = current normalization with oxide surface area. ^{b} Stability tests were examined using CV cycling, chronopotentiometry (CP), or chronoamperometry (CA).

(eqn (1)) was observed at 0.9 V vs. NHE in neutral $K_xH_{3-x}PO_4$ solutions (pH 7) and at 0.7 V vs. NHE in alkaline KOH (pH 13) solution[36,90,91] (Fig. 4(a and b)). After the delithiation, the OER engaged at 1.7 V (pH 7) and 1.5 V vs. RHE (pH 13). Unfortunately, OER activity was reduced during cycling due to surface deformation, from the layered structure to the non-active spinel structure at pH 7 (Fig. 4(c and d)) or amorphousness at pH 13 (Fig. 4(e)). Further, the OER activity and the catalytic stability of LTMO have been improved through doping foreign elements, nanostructuring catalysts, and in situ surface reconstruction during the OER. Table 1 shows representative examples of LTMO catalysts and summarizes their overpotential, Tafel slope, and stability.

3.3.1 Valence states of transition metals by alkali metal extraction. The intriguing LTMO characteristic is the tunable valence state of M^{n+} by extracting alkali metal ions, such as Li$^+$ and Na$^+$, from the LTMO[12,61] (Fig. 5(a)). This modulation of M^{n+} valence states tunes catalytic activity by altering the d-orbital, electronic band structure, and M^{n+}–O bond covalency, as discussed in Section 3.2. Cui and coworkers reported that delithiated LCO nanoparticles, denoted as De-LCO, obtained by 50% Li$^+$ extraction in organic electrolyte solutions, dramatically improved OER performance.[12,92] They suggested that the high-index crystalline surface, such as (104) of LCO, provided an

Li$^+$ extraction path, and the formed Co^{4+} acted as the main active site.[90,92] This behavior is associated with electronic structure changes upon forming Co^{4+}, such as enhancement of Co–O* electrophilicity (eqn (3)), Co–O covalency, and electronic conductivity (Fig. 1(c)). Delithiation of LCO in an organic medium or an aqueous electrolyte solution showed different OER activity. De-LCO prepared in an organic medium typically showed a lower overpotential (Fig. 5(b)), which was supported by identical results from various Li$^+$-incorporating LTMO (Fig. 5(b) inset). Among these LTMO, the equivalent mixed-layered oxide structures, incorporating Co, Ni, and Fe (De-LiCo$_{0.33}$Ni$_{0.33}$Fe$_{0.33}$O$_2$), outperformed the others with a small Tafel slope (35 mV dec^{-1}) and a low overpotential (295 mV @ 5 mA cm^{-2}) and better OER activity than the benchmark commercial Ir/C catalyst (46 mV dec^{-1} and 315 mV).

Similarly, the OER kinetics of NaCoO$_2$ was enhanced by forming Co^{4+} through the Na$^+$ deintercalation.[33,61,63] Cheng and coworkers suggested the increased V_O concentrations and improved electronic conductivity in Na$^+$ deintercalation. In addition, the optimum design was suggested to be ~40% Na$^+$ deintercalation states (i.e., Na$_{0.6}$CoO$_2$).[63] Ren and coworkers highlighted the role of Co–O covalency in Na$_x$CoO$_2$.[61] The O 2p band upshifted toward E_F with lower Na$^+$ content, resulting in stronger Co–O hybridization and participation of the oxygen
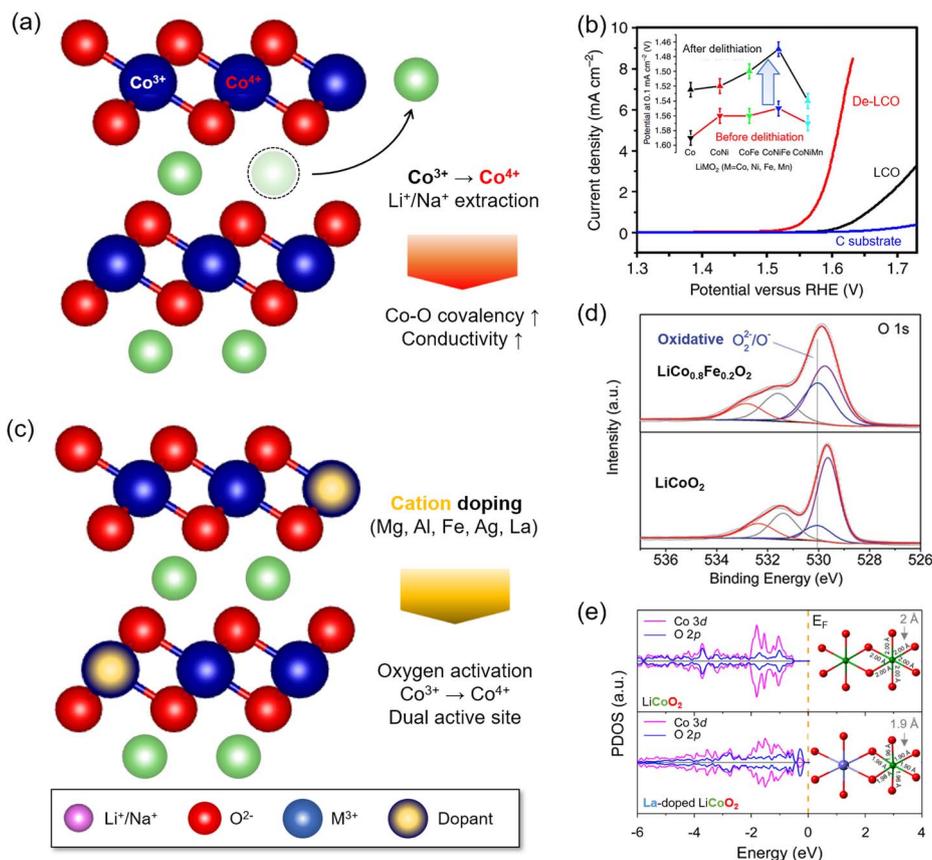
Fig. 5 Local structure modulation for OER enhancement of LTMO. (a) Schematic illustration of alkali metal ion extraction. (b) Linear sweep voltammograms (LSVs) of delithiated LCO (De-LCOs) and pristine LCO. The inset indicates the potential value at 0.1 mA cm^{-2} for various LTMO compositions before and after delithiation. Adapted with permission from ref. 12. Copyright 2014 Springer Nature. (c) Schematic illustration of foreign cation doping. (d) O 1s spectra from XPS analysis indicating the formation of highly oxidative oxygen species by Fe doping. Adapted with permission from ref. 37. Copyright 2015 John Wiley and Sons. (e) DFT simulation of the projected density of states and local geometry for LCO with and without La doping. Adapted with permission from ref. 47. Copyright 2019 American Chemical Society.

lattice in the OER. They are the central OER descriptors, as described in Section 3.2. Another important aspect was the short O–O distance in the CoO_6 unit, observed from $Na_{0.67}CoO_2$.[33] Due to the strong Co^{4+}–O^{2-} bond in the $R\bar{3}c$ space group, two O^{2-} ligands had <2.4 Å distance and easily formed the peroxide ion (O_2^{2-}) in leaving behind the V_O, which was similar to the LOM path in eqn (6). This peroxide evolved O_2 gas, and the OER overpotential was only 290 mV at 10 mA cm^{-2}.

3.3.2 Elemental doping. Foreign metal-ion doping can increase the active cations ratio and make new active sites on the transition metal oxide[46–48,78] (Fig. 5(c)). It affects the valence state of the host M^{n+},[37,48,64] the electronic structure,[78,93] the chemical properties of oxygen ligands,[94] and the symmetry of the lattice.[47,95] The electrochemically inert Al^{3+} doping into the layered $LiNiO_2$ structure stabilized Ni^{3+} in the NiO_2 slab and avoided undesired Ni^{3+} reduction and phase transition.[96] In the absence of Al^{3+}, the Ni^{3+} of $LiNiO_2$ underwent disproportionation to Ni^{2+} and Ni^{4+}, causing a cation mixing disorder between Ni^{2+} and Li^+.[97] Thus, the stable Ni^{3+}/Ni^{4+} redox process was the reason for the improved OER activity. As another example, doping LCO nanosheets with divalent Mg^{2+} preserved the Co^{4+} state. The existing Co^{4+} increased the Co–O covalency as the Co

3d and O 2p bands were largely overlapped, showing a 329 mV overpotential at 10 mA cm^{-2}.

The impurity of Fe ions in the electrolyte solution often significantly improved the OER, and this behavior developed the idea of Fe ion doping to layered double hydroxide (LDH) or perovskite oxides.[37,65,66] In the LDH electrocatalysts (*e.g.*, nickel (oxy)hydroxide, NiOOH), the Fe dopant served as dynamic OER active sites as Fe ions were dissolved and deposited in LDH repeatedly during the OER.[98–100] For the perovskite $LaNiO_3$, the incorporation of Fe ions distorted the local lattice structures, and the occupied Fe 3d states beneath the E_F accelerated charge transfer from M^{3+}–$O(OH^*)^-$ to M^{4+}–OO^{*2-}.[93,101] Shao and coworkers showed that substituting 20% Co with Fe in LCO, thus forming $LiCo_{0.8}Fe_{0.2}O_2$, reduced the overpotential to 350 mV at 10 mA cm^{-2}.[37] X-ray photoelectron spectroscopy (XPS) revealed partial oxidation of Co^{3+} to Co^{4+} and an increased amount of O_2^{2-} or O^-, which might be generated from partial oxidation of the O^{2-} ligand near 530.1 eV (Fig. 5(d)). The electrophilicity of the oxygen ligand and V_O generation at the surface caused enhancement of OER activity (Section 3.2.4).[50,94,102–104] In addition, the Fe dopant increased the electronic conductivity, demonstrated by the reduced charge

transfer resistance. Similar effects from the Fe dopant were also found in $Na_{0.86}Co_{0.95}Fe_{0.05}O_2$ (ref. 65) and $Na_{0.67}Mn_{0.5}Co_{0.3}$-$Fe_{0.2}O_2$,[66] where both Co and Fe acted as OER active sites.[105,106]

Because the dopant size was often mismatched to the host M^{n+} size of catalysts, the foreign ion doping imposed the strain on the surface lattice. La doping to LCO shortened the Co–O length (<2 Å) in the CoO_6 octahedral unit and distorted the symmetry[47] (Fig. 5(e)). This mechanical strain upshifted the O 2p band centre and induced stronger Co–O covalency. As a result, La doping in LCO resulted in a 330 mV overpotential at 10 mA cm^{-2}, which was better than that of LCO (440 mV). A similar effect was also observed from Ag-doped $Na_{0.7}CoO_2$.[62]

3.3.3 Nanostructuring. Nanostructured catalysts provide higher surface areas and enlarged active sites. Thus, surface modifications modulate the electronic structure significantly. Two-dimensional LCO nanosheets denoted as LCO-NS were synthesized by hydrothermal lithiation of $Co(OH)_2$ or CoOOH, or exfoliation of bulk LCO particles[67–70,92] (Fig. 6(a)). These synthetic processes imposed mechanical stress and caused defects to develop. Li and coworkers synthesized a 2–3 nm thickness LCO-NS that included 5–6 CoO_2 layers (Fig. 6(b)) and

demonstrated the formation of numerous V_O using XPS and electron paramagnetic resonance (EPR).[67] High and low spin states of Co were mixed in LCO-NS by forming Co^{4+} (Fig. 6(c)). As a result, the enhanced electronic conduction and electrophilicity contributed to a 410 mV OER overpotential at 10 mA cm^{-2} (Section 3.2).

Sun and coworkers designed atomic-layered defect-rich LCO, denoted as AD-LCO, using a mechanical shear-assisted exfoliation method.[68] The 3–5 nm thick AD-LCO contained cationic Co vacancies and distorted CoO_6 (Fig. 6(d and e)). In addition, as the Co valence states became higher (4+), the Co–O covalency became stronger. Modulating the electronic structure decreased the OER overpotential to 280 mV at 10 mA cm^{-2} (Fig. 6(e and f)).

Along with the nanostructured OER catalysts, the effects of micro-structured substrates[69] or decorated nanoparticles were investigated.[70,107] Hierarchical growth of LCO-NS on carbon cloth formed microstructures and showed a 289 mV overpotential of the OER at 10 mA cm^{-2} after delithiation.[69] Sun and coworkers attached Pt nanoparticles (around 2.2 nm diameter) to LCO-NS (10–25 nm thickness) and demonstrated a 285 mV OER overpotential at 10 mA cm^{-2} (ref. 70) (Fig. 6(h–k)). The
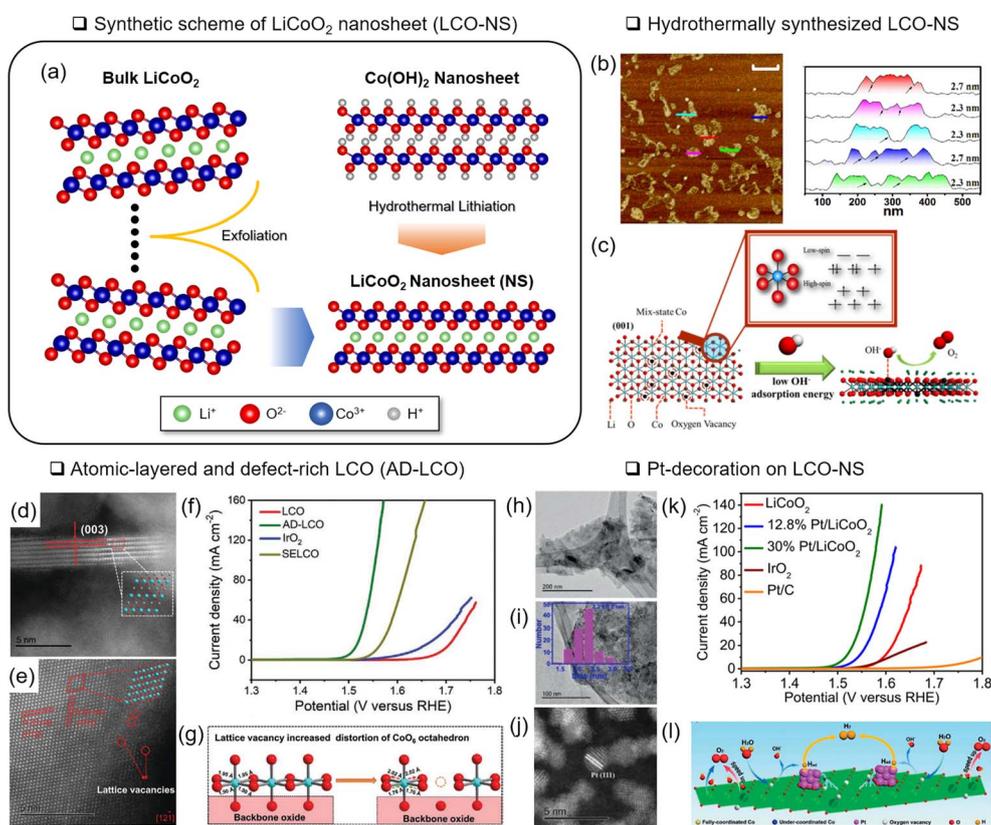
Fig. 6 Nanostructuring of LCO. (a) Schematic illustration of an LCO nanosheet (LCO-NS) obtained by an exfoliation and hydrothermal lithiation method. (b) Atomic force microscopy analysis of LCO-NS. (c) Schematic illustration of LCO-NS with rich V_O and multiple spin states of Co. Reproduced with permission from ref. 67. Copyright 2017 American Chemical Society. Scanning TEM image of atomic-layered and defect-rich LCO (AD-LCO) for (d) the edge step and (e) basal plane. (f) Corresponding LSV analysis with various reference materials. (g) Schematic illustration of the cation vacancy effect on AD-LCO for the OER. Reproduced with permission from ref. 68. Copyright 2022 John Wiley and Sons. (h–j) Structure analysis of Pt-decorated LCO-NS and TEM analysis of (h) LCO-NS and (i) anchored Pt nanoparticles. (j) Corresponding STEM image. (k) LSV analysis of Pt/LCO with various Pt loading. (l) Schematic illustration of the synergistic effect of Pt/LCO. Reproduced with permission from ref. 70. Copyright 2020 John Wiley and Sons.

charge transfer between Pt and Co^{3+} was presumed to form Pt^{2+}, Co^{2+}, and V_O. This V_O and under-coordinated Co in LCO-NS served as the active OH^- adsorption site (Fig. 6(l)).

3.3.4 Regulating surface reconstruction. Understanding surface reconstructions of LTMO before and during the OER is pivotal to addressing the active sites.[89,91] Surface reorganization can be controlled by modulating the active cation ratios, which adjusts the O 2p band centre and the valence state of M^{n+} (see Section 3.2). In addition, OER-active phases were newly formed during the OER and performed stably.[34,44,57,108] Thus, in-depth analyses of the newly formed amorphous phases were necessary to identify the new catalytic sites.

Byon and coworkers demonstrated the surface reconstruction of De-LCO by inserting foreign alkali metal ions such as Na^+, K^+, and Cs^+ during the OER process and investigated the related mechanisms.[36] Using NaOH or KOH electrolyte solutions, hydrated Na^+ or K^+ was inserted into De-LCO, creating the

$Li_{0.25}Na_{0.33}CoO_2 \cdot (H_2O)_{0.04}$ and $Li_{0.33}K_{0.17}CoO_2 \cdot (H_2O)_{0.37}$ structures, respectively. The OER activity of $Li_{0.33}K_{0.17}CoO_2 \cdot (H_2O)_{0.37}$ was better than that of $Li_{0.25}Na_{0.33}CoO_2 \cdot (H_2O)_{0.04}$, because less K^+ insertion induced higher Co^{4+} concentration (Fig. 7(a)). These bulk structural reconstructions enhanced the Co^{4+} concentration and the Co–O covalency, and the AEM governed the OER process. In comparison, little Cs^+ was intercalated into De-LCO in the CsOH electrolyte solution, and the resulting $Li_{0.55}Cs_{0.03}CoO_2 \cdot (H_2O)_{0.07}$ underwent negligible bulk phase transition. This shallow Cs^+ insertion preserved the bulk LCO structure, causing better OER stability than the K^+ and Na^+ intercalations. In addition, $Li_{0.55}Cs_{0.03}CoO_2 \cdot (H_2O)_{0.07}$ showed the best OER activity despite the small Co^{4+} concentrations (Fig. 7(b)). This was attributed to the surface strain caused by large-size Cs^+, leading to the CoO_2 slab edge bending (Fig. 7(c and d)). Its strong pH dependency indicated LOM as the main OER mechanism, distinguished from the above K^+ and Na^+ intercalated catalysts.
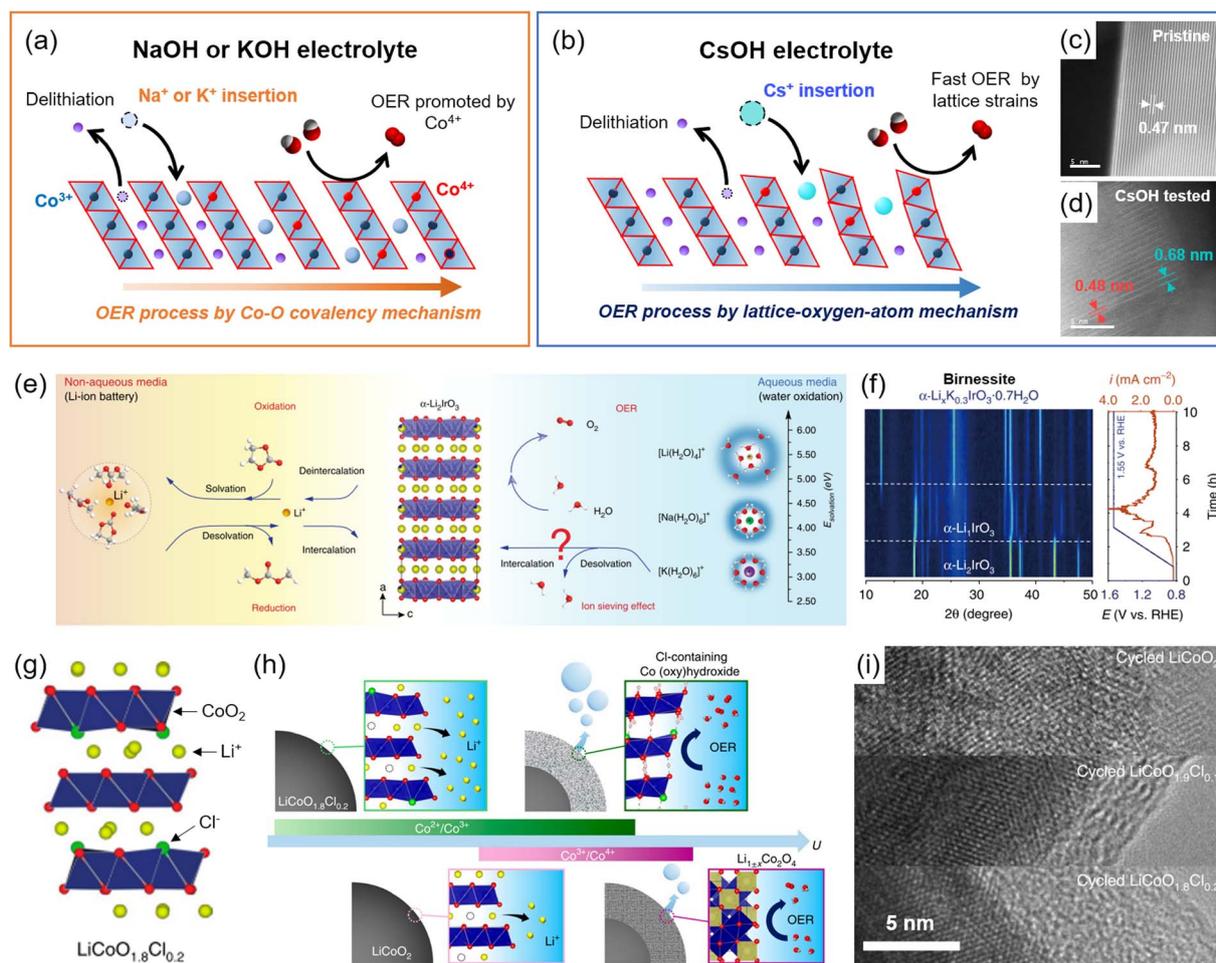
Fig. 7 Surface reconstructions on LCO during the OER. (a and b) Schematic illustration of foreign alkali metal ion insertion on the Li^+ vacant site with (a) small size ions (Na^+ and K^+) exhibiting OER enhancement from different Co^{4+} development and covalency, and (b) large size Cs^+ following LOM. Comparison of the interlayer distances of (c) pristine and (d) OER-tested LCO after Cs^+ insertion. Adapted with permission from ref. 36. Copyright 2022 Royal Society of Chemistry. (e) Schematic illustration of hydrated K^+ intercalation on α-Li_2IrO_3. (f) *Operando* XRD analysis for birnessite phase formation during the OER of α-Li_2IrO_3. Reproduced from ref. 72. Copyright 2020 Springer Nature. (g) Crystal structure of Cl-doped LCO, $LiCoO_{1.8}Cl_{0.2}$. (h) Schematic illustrations of the surface reconstruction of LCO and $LiCoO_{1.8}Cl_{0.2}$ during the OER. (i) Corresponding TEM images after OER cycling. Reproduced with permission from ref. 34. Copyright 2021 Springer Nature.

Grimaud and coworkers also reported similar phenomena for the layered α-Li$_2$IrO$_3$ (ref. [71]) (Fig. 7(e)). The delithiated α-Li$_2$IrO$_3$ produced an α-Li$_1$IrO$_3$ structure, which had a high-valence state (5+) of Ir^{5+}, and induced hydrated K$^+$ insertion, promoting chemical OER. During this process, α-Li$_x$K$_{0.3}$IrO$_3$·0.7H$_2$O was entirely converted to a birnessite structure and showed OER activity[109] (Fig. 7(f)). The hydrated K$^+$ continuously underwent reversible deintercalation and intercalation during the OER process, and this behavior was not observed in Li$^+$ and Na$^+$ electrolytes.

Lim and coworkers doped Cl$^-$ into LCO, forming LiCoO$_{1.8}$Cl$_{0.2}$, and induced structural reconstruction[34] (Fig. 7(g)). The introduction of Cl$^-$ reduced Co^{3+} to Co^{2+} and caused the irreversible Co^{2+}/Co^{3+} redox at <1.4 V vs. RHE through delithiation. As a result, a low redox potential developed a new pathway of surface reconstruction (Fig. 7(h)). The LiCoO$_{1.8}$Cl$_{0.2}$ formed an amorphous and Cl-doped cobalt (oxy)hydroxide surface during the OER, which prevented the Li$^+$ extraction from the bulk structure and terminated the reconstruction process. This result contrasted with the continuous surface reconstruction of the LCO, becoming the spinel phase of Li$_{1\pm x}$Co$_2$O$_4$ (Fig. 7(i)). Thanks to the highly OER-active Cl-doped cobalt (oxy)hydroxide and the increased conductivity of LiCoO$_{1.8}$Cl$_{0.2}$ in the bulk structure, the reconstructed catalysts exhibited a 270 mV overpotential at 10 mA cm^{-2}.

4. LTMO as cathodes for aqueous LiBs

In this LiB section, we discuss the Li$^+$ intercalation and deintercalation process in LTMO electrodes, which competes with H$^+$ intercalation in an aqueous electrolyte solution.

In non-aqueous media, LTMO serves as the stable cathode in LiBs. The representative LCO electrode provides a capacity of 140 mA h g^{-1} by extracting 50% of total Li$^+$, which occurs at around 4.0 V vs. Li/Li$^+$.[124] Layered NCM further improves Li$^+$ storage capacity by storage of two Li moieties through Ni^{2+}/Ni^{4+} redox chemistry. Mn helps maintain the thermal stability of NCM, while Co provides high electronic conductivity.[125] In addition, a small Co content in NCM compared to that in LCO diminishes the cost and toxicity. NCM811 (811 represents the ratio of transition metals Ni, Co, and Mn) has 200 mA h g^{-1} capacity and 3.88 V (vs. Li/Li$^+$) charging voltage.[126,127] Nonetheless, non-aqueous LiBs suffer from the risk of catching fire and the high cost of electrolyte solutions. They are particularly unsuitable for grid-scale ESSs.

An aqueous electrolyte solution has been introduced in LiBs to tackle this issue. Dahn and coworkers first reported rechargeable aqueous LiBs with 5 M LiNO$_3$ electrolyte in 1994.[128] However, the narrow electrochemical potential window of water, thermodynamically in the range of 2.62–3.85 V vs. Li/Li$^+$ (converted from 0.0–1.23 V vs. RHE), restricts the use of graphite and metallic Li electrodes operating at 0–0.1 V vs. Li/Li$^+$. It is also the reason for the significantly low energy density. For the cathode side, LTMO is unstable in water because Li$^+$ intercalation competes with H$^+$ intercalation, which originates from the dissociated water in neutral and weakly alkaline conditions. Thus, the interfacial reaction of LTMO with water provides significant challenges in aqueous LiBs. Here, we focus on the LTMO-based Li$^+$/H$^+$ insertion chemistry in aqueous cathodes.

4.1. H$^+$ intercalation competing with Li$^+$ intercalation in salt-in-water electrolyte solutions

The layered-structure LCO undergoes Li$^+$ intercalation and deintercalation below the OER potential and forms Li$_{1-x}$CoO$_2$ where x is between 0.5 and 1. However, LiV$_3$O$_8$|LCO cells with a saturated LiNO$_3$ electrolyte in water provided only 55 mA h g^{-1} capacity at an average charging/discharging potential of 4.38 V vs. Li/Li$^+$, where LiV$_3$O$_8$ and LCO are the anode and cathode, respectively[114,115] (Table 2). Water causes low capacity and rapid capacity fading for cycling. As another example, NCM electrodes had higher theoretical capacity than LCO and comparable charging/discharging voltages. However, an LiNi$_{0.81}$Co$_{0.19}$O$_2$ or NCM111 electrode coupled with an LiV$_3$O$_8$ anode delivered only 45 mA h g^{-1} with 1–2 M Li$_2$SO$_4$ aqueous solution.[117,118] Low NCM capacities relative to LCO were due to their extreme water sensitivity and severe Ni ion dissolution.[126]

There were several demonstrations of adverse water effects on LTMO. Thin LCO electrodes suffered from H$_2$O vapor in all-solid-state Li cells, resulting in 21 mA h g^{-1} capacity for the first cycle, which was only 20% of the capacity for the H$_2$O vapor-free LCO capacity[13] (Fig. 8(a and b)). The depth profile evaluated by resonant nuclear reaction analysis showed the presence of hydrogen in 20–30 nm depth of LCO (Fig. 8(c)). In addition, when NCM532 (without delithiation) was stored at high humidity over one month, its capacity was reduced;[129] galvanostatic testing in the non-aqueous electrolyte solution exhibited a lower charging capacity of this NCM532 at 166 mA h g^{-1} (vs. 198 mA h g^{-1} for the fresh NCM532) and lower coulombic efficiency (CE, indicating reversibility during charging and discharging processes) at 86.9% (vs. 90.4% for the fresh one). This was attributed to Li$^+$ exchange with H$^+$ during the storage period. Li$^+$ migrated outward of NCM and formed LiOH and Li$_2$CO$_3$ on the electrode surface, while H$^+$ from humid air moved inside LCO. The resulting structural deformation destabilized NCM. However, the H$^+$ insertion rate for non-delithiated NCM was slower than for the delithiated one.[117,118] It should also be noted that H$^+$ intercalation is preferred in the close-packed hexagonal stacking LTMO compared to spinel (e.g., LiMn$_2$O$_4$) and olivine (e.g., LiFPO$_4$) structures.[130]

The first-principles density functional theory (DFT) calculations showed that when H$^+$ is inserted between the CoO$_2$ layers of the delithiated LCO, it is bound to the CoO$_2$ lattice and forms an O–H covalent bond[131,132] (Fig. 8(e and f)). H$^+$ and Li$^+$ are stabilized at different stacking sites; H$^+$ is inserted into the prismatic sites, while Li$^+$ is located in the octahedral sites of the delithiated LCO.[133] Unfortunately, the O–H bond formation at the prismatic sites raises the energetic barrier of Li$^+$ diffusion and restricts the Li$^+$ diffusion pathway.[132] Conversely, it is also predicted that the O–H bond prevents the oxidation of the oxygen lattice, suppressing OER activity related to LOM (see

Table 2 Aqueous LiB performances with LTMO cathodes and various electrolytes

Cell types	Cell configuration	Electrolyte[a]	E range (V)	J or C-rate[b]	Capacity retention	Initial charge capacity (mA h g⁻¹)	CE (%)	Cycle number	Ref.
Half cell	LiCoO₂ (Ag/AgCl RE, Li₀.₅Mn₂O₄ CE)	5 M LiNO₃	3.59–4.19 (vs. Li⁺/Li)	1C	—	105	99.70	90	110
	LiCoO₂ (Ag/AgCl RE, Li₀.₅Mn₂O₄ CE)	5 M LiNO₃	3.59–4.24 (vs. Li⁺/Li)	1C	82–86%	135	82.00	200	111
	LiNi₀.₆Mn₀.₂Co₀.₂O₂ (Ag/AgCl RE, Pt foil CE)	20 M LiTFSI	3.25–4.45	20 mA g⁻¹	—	152	81	3	112
Full cell	Activated carbon|LCO	0.5 M Li₂SO₄	0–1.8	7C	—	143	92.50	40	113
	LiV₃O₈||LiCoO₂	Sat'd LiNO₃	0.5–1.5	1C	65%	55	—	40	114
	LiV₃O₈||LiCoO₂	Sat'd LiNO₃	0.5–1.5	0.2 mA cm⁻²	—	60	—	12	115
	Li metal(GPE[c] + LISICON[d]|| LiCoO₂	0.5 M Li₂SO₄	3.5–4.3	150 mA g⁻¹	—	130	—	20	116
	Li₉/₇₋ₓNb₂/₇Mo₃/₇O₂|LiCoO₂	3 m Li₂SO₄	0–1.5	0.5C	74%	44	99.80 (20th)	500	17
	LiV₃O₈||LiNi₀.₈₁Co₀.₁₉O₂	1 M Li₂SO₄	0.5–2	1 mA cm⁻²	40%	45	—	100	117
	LiV₃O₈||LiNi₁/₃Co₁/₃Mn₁/₃O₂	2 M Li₂SO₄	0.5–1.5	0.2 mA cm⁻²	54.70%	55.2	—	10	118
	LiV₂.₉Ni₀.₀₅Mn₀.₀₅O₈|LiNi₁/₃Co₁/₃Mn₁/₃O₂	1 M LiNO₃, 5 M LiNO₃, Sat'd LiNO₃	0.5–1.5	0.5C	65%	98.2	92	50	119
	LiV₃O₈|10 wt% PPy–LiNi₁/₃Co₁/₃Mn₁/₃O₂	5 M LiNO₃	0–1.4	0.2 mA cm⁻²	71%	70	—	50	120
	Li₄Ti₅O₁₂|Ni₀.₈Mn₀.₁Co₀.₁O₂	40 m LiTFSI + 20 m EMImTFSI[e]	0.8–2.75	1C	—	~67	99.4	300	121
	Mo₆S₈|LiCoO₂	21 m LiTFSI + 0.1 wt% TMSB[f]	1–2.5	2.5C	—	~40	—	1000	122
	Li₄Ti₅O₁₂|LiCoO₂	Li(TFSI)₀.₇(BETI)₀.₃·2H₂O	1.6–2.6	10C	75%	55.3	~100	200	123

[a] Sat'd = saturated. [b] J stands for current density. [c] GPE: PVDF (poly(vinyl difluoride))–PMMA (poly(methyl methacrylate))–PVDF saturated in 1 M LiClO₄. [d] LISICON: Li₂O–Al₂O₃–SiO₂–P₂O₅–TiO₂–GeO₂. [e] EMImTFSI: 1-ethyl-3-methylimidazolium TFSL. [f] TMSB: tris(trimethylsilyl) borate.
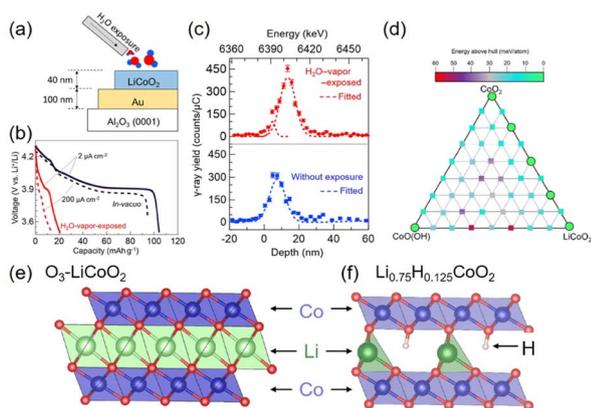
Fig. 8 Adverse water effect on LCO. (a) Schematic illustration of H_2O-vapor treatment of the LCO electrode. (b) Discharge voltage profile of H_2O-vapor exposed LCO (red) and pristine LCO (black) with the current of 2 and 200 $\mu A\ cm^{-2}$ for solid and dashed lines, respectively. Li_3PO_4 solid electrolyte and metallic Li anode were used. (c) Hydrogen depth profile of 40 nm LCO film from resonant nuclear reaction analysis. Reproduced with permission from ref. 13. Copyright 2023 American Chemical Society. (d) Energies above hull calculated by PBE + U for the phase diagram (0 K) of the $H_yLi_xCoO_2$ ($x + y \leq 1$) structure. (e) O3 structure of LCO. (f) Partial stacking displacement of $Li_{0.75}H_{0.125}CoO_2$ with Co (blue), O (red), and Li (green). Adapted with permission from ref. 133. Copyright 2021 American Chemical Society.

Section 3).[131] The computational model reveals the phase transition from O3 to P3 when $Li_{0.75}H_{0.125}CoO_2$ is formed. However, this transformation is incomplete because the octahedral site of Li^+ is pronouncedly distorted, and a high concentration of vacancies appears (Fig. 8(d)). It turns out that the total concentrations of Li^+ and H^+ cannot become unity by forming vacancies.[133]

In aqueous LiBs, water ($\sim$55 M) is an unlimited H^+ source in an aqueous medium compared to a limited Li^+ from the electrolyte (typically $\sim$1 M in a salt-in-water system). Because H^+ has a smaller volume size and faster mobility than Li^+, it damages the LTMO structure seriously. The fatal H^+ effect was found in low pH solutions and even in neutral conditions.[16] LCO underwent significant capacity loss in the initial cycles at pH < 7. In contrast, better charging and discharging cyclability in LCO were observed at pH > 9 with 1 m (mol kg^{-1}) Li_2SO_4.[17,132] However, because a strong alkaline solution engendered the OER and the LTMO served as OER catalysts in this condition, the pH of the aqueous electrolyte solutions was typically adjusted to a mildly alkaline condition (pH 9–11).[16]

To shed light on the H^+ insertion contending with Li^+, it is imperative to understand interfacial reactions at the aqueous electrolyte solutions/LTMO surface. Above the point of zero charge (PZC) or applied positive bias, water and anions sit on the topmost LTMO surface, called the inner Helmholtz plane (IHP), and form a few interfacial layers regime. The water molecules are the majority in the IHP and become the potential source of H^+. By comparison, anions of electrolyte salt are minor in the typical salt-in-water electrolyte solution. Byon and coworkers recently revealed that anions protected the LTMO surface from the H^+ insertion. To demonstrate the anionic

electrolyte effects, sulfate (SO_4^{2-}), nitrate (NO_3^-), perchlorate (ClO_4^-), and bistriflimide ($TFSI^-$) were examined with 0.5–1 m concentrations.[17] None of these anions either formed a cathode electrolyte interface (CEI) or significantly changed the solution pH. However, LCO cell performances were significantly different. Cyclability with 0.5 m Li_2SO_4 outperformed, revealing the constant capacity for 10 cycles (Fig. 9(a)). Electrochemical impedance spectroscopy (EIS) showed a single semicircle, indicating the Li^+ charge-transfer resistance during the charging and discharging process (Fig. 9(c)). In contrast, $TFSI^-$ exhibited a pronounced capacity decay under the same condition (Fig. 9(b)). Interestingly, EIS demonstrated additional semicircles at the low-frequency region, which belonged to H^+ insertion into LCO (Fig. 9(d)). NO_3^- and ClO_4^- also showed H^+ charge-transfer resistances in EIS, which were, however, moderate compared to $TFSI^-$. These H^+ inserting resistances corresponded to capacity decays for 100 cycles, verifying that H^+ was the central source for LCO degradation (Fig. 9(e)). The anion-dependent LCO stability is presumably explained by the Hofmeister series and kosmotropic traits. SO_4^{2-} has a strong kosmotropic character,[17] namely, the presence of SO_4^{2-} in water preserves the hydrogen-bond strength and induces the ordered ice-like structure. Thus, the H^+ dissociation is likely difficult due to the strong hydrogen-bonding water network. In sharp contrast, the weak kosmotropic $TFSI^-$ (i.e., the strongest chaotropic anion) attenuates the hydrogen-bond strength in water and induces disordered water structures, where H^+ dissociation is possibly more favorable.

Further, in situ electrochemical surface-enhanced infrared absorption spectroscopy (SEIRAS) revealed the role of SO_4^{2-} adsorption at the LCO surface and IHP. SO_4^{2-} was coordinated with the LCO surface to form bidentate coordination (C_{2v} point group), distinct from a typical tetrahedral (T_d) free SO_4^{2-} in the bulk solution (Fig. 9(f), C_{2v}: 951, 1136, 1200 cm^{-1} and T_d: 1095 cm^{-1}). It demonstrated the complete SO_4^{2-} adsorption on the LCO surface, where the water contacts and possible H^+ access were prevented. By comparison, $TFSI^-$ adsorption was not evidenced in the IHP using electrochemical SEIRAS. Another concern was the H^+ access at slightly below the PZC when SO_4^{2-} was desorbed from LCO. This condition was often included before reaching the cut-off potential of galvanostatic tests and reasoned for severe capacity loss. Indeed, the SO_4^{2-} vibration from the T_d structure (1095 cm^{-1}) was enhanced, while C_{2v}-associated vibrations were attenuated below 0.2 V vs. Ag/AgCl during discharge in electrochemical SEIRAS (Fig. 9(f)). Mean-field quantum mechanics/molecular mechanics (QM/MM) simulation predicted that SO_4^{2-} was more concentrated on the LCO surface than other anions (Fig. 9(g)). Below the PZC, Li^+ is primarily distributed on LCO and hard Lewis base SO_4^{2-} easily forms ion pairing with hard Lewis acid Li^+ according to the hard and soft acids and bases (HSAB) concept. Thus, SO_4^{2-} stays on the LCO surface and avoids H^+ insertion. In sharp contrast, the soft Lewis base $TFSI^-$ is not closely associated with Li^+, resulting in the exposure of delithiated LCO to water and H^+.

From the above lesson, we can also understand the better performance of LTMO in aqueous LiBs with higher

concentrations of electrolyte salts.[110,134] The increased anion concentrations give rise to an anion-rich IHP and suppress the H^+ insertion. A 3 m Li_2SO_4 solution extended the electrochemical potential window towards the positive potential compared to a 0.5 m Li_2SO_4. Further, a 3 m Li_2SO_4 had the widest potential window compared to 6 m $LiNO_3$, 5 m $LiClO_4$, and 6 m LiTFSI. This was attributed to the strong SO_4^{2-} adsorption which led to forming bidentate coordination with the LCO surface compared to other anions.[17] LCO with 3 m Li_2SO_4 electrolyte solution showed 87% capacity retention for 1500 cycles, which was better than the 66% retention with 7.5 m $LiNO_3$.[134] It was also reported that a 2–3 nm CoO layer was formed on LCO after 500 cycles with 3 m Li_2SO_4 solution, because of a chemical reaction between LCO and water. This surface layer delayed the LCO structural degradation. In

comparison, LCO with 1 M $LiNO_3$ electrolyte created a thicker (5–6 nm) and amorphous CoO layer.[134]

A similar approach was attempted at NCM. The electrochemical performance of NCM111 was examined with 1 M $LiNO_3$ and saturated (7.5 m) $LiNO_3$ in water.[119] The anodic and cathodic peak separating potential ($E_{p,p}$) in CV was 0.356 and 0.25 V for 1 M and saturated $LiNO_3$, respectively. It revealed more undesirable chemical reactions with lower electrolyte concentration. $LiV_{2.9}Ni_{0.05}Mn_{0.05}O_8$|NCM111 cells with the saturated $LiNO_3$ solution delivered an initial capacity of 98.2 mA h g^{-1} at 0.5C and 62.8 mA h g^{-1} at 3C.

Apart from anions, artificial protective layers were also developed.[16] The coating of the lithiated Nafion layer protected the LCO during the initial cycles. The hydrophobic domain of Nafion prevented water access to LCO, while the hydrophilic
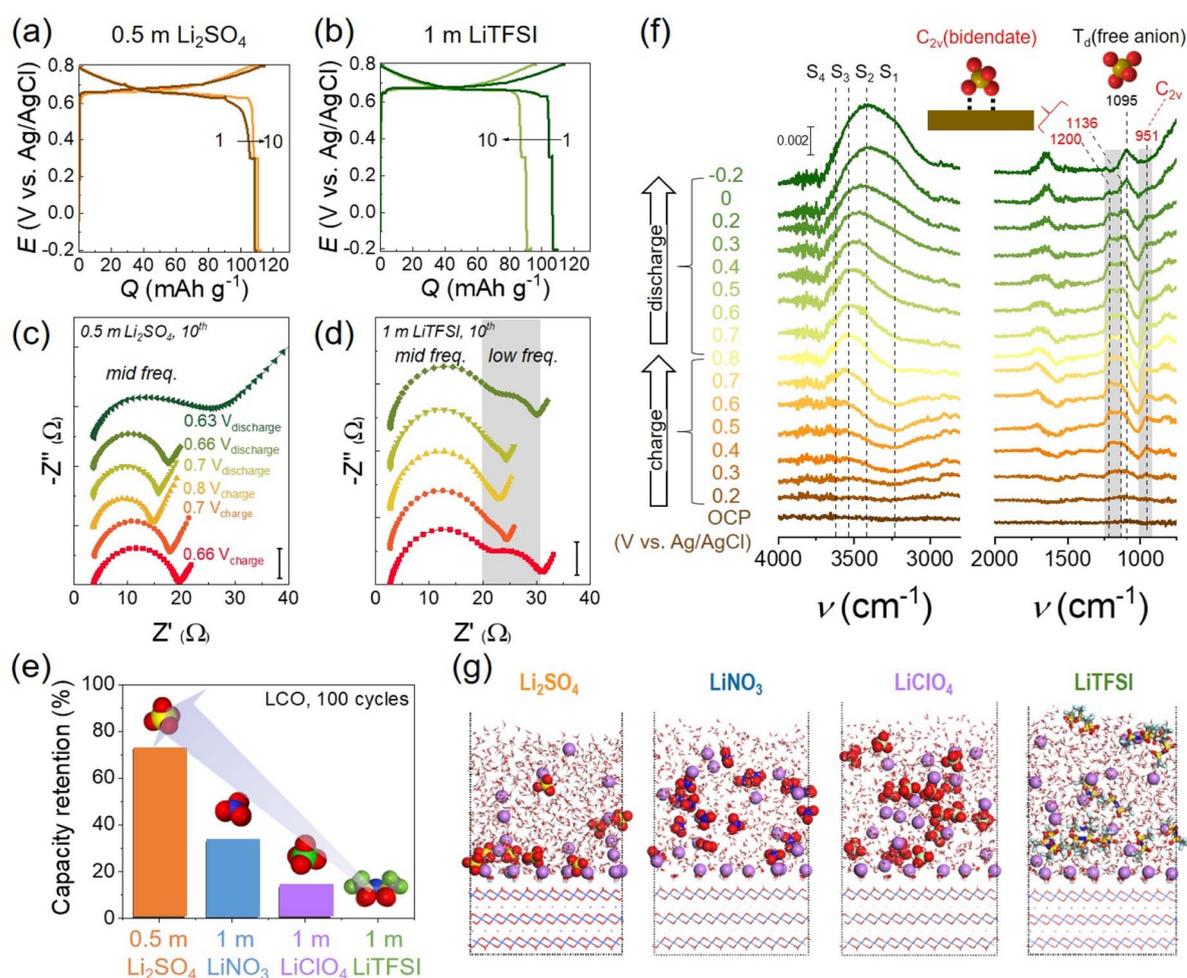
Fig. 9 Anion effects on LCO in salt-in-water electrolytes. (a and b) The 1st and 10th galvanostatic cycles of the LCO half-cell at 0.5C in (a) 0.5 m Li_2SO_4 at pH 9.6 and (b) 1 m LiTFSI at pH 8.5. (c and d) Corresponding Nyquist plot obtained from EIS measurement during the 10th cycle in (c) 0.5 m Li_2SO_4 and (d) 1 m LiTFSI. EIS was measured during charging at 0.66 V, 0.7 V, and 0.8 V and subsequent discharging at 0.7 V, 0.66 V, and 0.63 V (Li_2SO_4 only). (e) The capacity retention of LCO for 100 cycles with different electrolytes. (f) In situ electrochemical SEIRAS spectra with 0.5 m Li_2SO_4. Ice-like water structures are designated as S_1 and S_2, liquid-like water structures as S_3, and disordered free water molecules as S_4, respectively. The peak at 1095 cm^{-1} is assigned to the T_d point group of a free anion, SO_4^{2-}, and the peaks at 951, 1136, and 1200 cm^{-1} are attributed to the bidentate coordinated C_{2v} point group of SO_4^{2-}. (g) QM/MM simulations of Li$^+$ and anion adsorption on LCO having a negative surface charge ($\sigma = -11.5$ μC cm^{-2}). Li$^+$ (purple), O (red), S (yellow), C (gray), F (cyan), N (blue), and Cl (light green). Reproduced with permission from ref. 17. Copyright 2023 American Chemical Society.

part, including the sulfonate group, played the role of the Li$^+$ ion channel, which enhanced cyclability for the first 30 cycles with 1 m LiTFSI in water. However, the Nafion layer eventually underwent water swelling during long-term cyclability, causing inevitable LCO deformation. Polypyrrole (PPy) conducting polymer was utilized as a protective layer on NCM111.[120] It showed an initial capacity of 70 mA h g^{-1} and 70% capacity retention for 50 cycles, compared to PPy-free NCM111 which exhibited 60 mA h g^{-1} initial capacity and ~33% capacity retention for 40 cycles. The formed 2 nm thick spinel-Co$_3$O$_4$ layer on layered LCO also served as a protective layer and prevented Co ion dissolution.[135] The Co$_3$O$_4$-LCO delivered a 1st cycle capacity of 83.6 mA h g^{-1} at 0.1 A g^{-1} and 84.5% capacity retention for 100 cycles with 1 M Li$_2$SO$_4$ in water. In comparison, Co$_3$O$_4$-free LCO exhibited a capacity of 84.8 mA h g^{-1} and 70.5% retention.

4.2. Diminishing water activity in water-in-salt electrolytes

Despite numerous attempts at electrode surface protection, LTMO underwent structural deformation and poor long-term cycling performance. An alternative and more fundamental strategy is to significantly diminish the source of H$^+$, *i.e.*, water. Dissolving extremely high electrolyte concentrations can reduce water volume remarkably, which causes decreased water activity (*i.e.*, concentration). This concept was developed by discovering the dissolution of 21 m LiTFSI in water.[136] It seemingly forms a water-in-salt electrolyte (WiSE), where the Li$^+$ solvation structures are entirely changed, and Li$^+$ and anion interactions are stronger.

As water activity is significantly reduced, most water molecules solvate numerous Li$^+$ ions, while the concentration of free water is low[136] (Fig. 10(a)). In addition, Li$^+$ is coordinated with a few water molecules instead of being shielded by primary and secondary water shells, which leads to strong Li$^+$ and TFSI$^-$ attraction and the formation of aggregated ion pairs. Computational simulations and femtosecond IR spectroscopic observations demonstrated two separated domains, water channel and aggregated ion networks, in the bulk electrolyte[137-139] (Fig. 10(b)). In this heterogeneous solvation structure, Li$^+$ transport occurred in a bulk-like water molecule channel, explaining the higher ionic conductivity (~9.5 mS cm^{-1} at 25 °C) than expected due to high viscosity.[140] At the electrode surface, molecular dynamics (MD) simulations envisioned that the aggregated ion pairs are mostly occupied in the IHP while the water molecules were located away from the electrode surface[141-143] (Fig. 10(c)). Experimentally, atomic force microscopy (AFM) force measurements detected two layers of thickness on gold electrodes, 4.3 and 6.4–6.7 Å at 0.3 V *vs.* Ag/Ag$^+$. They were assigned to the TFSI$^-$-rich layer and aggregated ion pair clusters ([Li(H$_2$O)$_x$]$^+$([TFSI]$^-$)$_y$), respectively[141] (Fig. 10(d)). These aggregated ion pairs had large sizes and were loosely bound to the surface. In comparison, the negatively charged
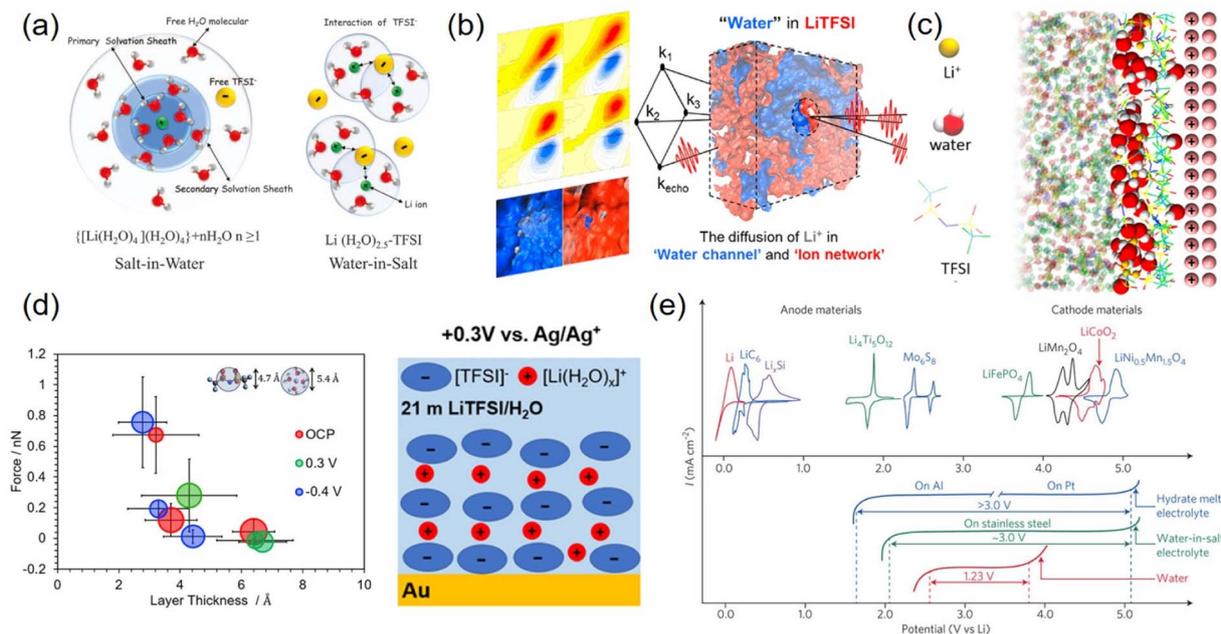
Fig. 10 Water-in-salt electrolytes in bulk solution and at the interfacial region and electrochemical voltage. (a) Schematic illustration of the Li$^+$ primary solvation sheath in salt-in-water (left) and water-in-salt electrolytes (right). Reproduced with permission from ref. 136. Copyright 2015 The American Association for the Advancement of Science. (b) Nano-heterogeneous domain of H-bond networks in water and ion networks obtained by 2D-IR measurements. Reproduced with permission from ref. 137. Copyright 2018 American Chemical Society. (c) Molecular dynamics (MD) simulation of 21 m LiTFSI with a positively charged (100) gold electrode. Reproduced with permission from ref. 142. Copyright 2018 American Chemical Society. (d) Diagram of layer thickness *vs.* force imposed by AFM for 21 m LiTFSI on (111) textured Au at OCP, 0.3 V, and −0.4 V (left). Schematic illustration of chemical species in the electrochemical double layer at 0.3 V (right). Reproduced with permission from ref. 141. Copyright 2020 American Chemical Society. (e) CV of various anode and cathode materials (top) and LSV of hydrate-melt electrolyte, water-in-salt electrolyte, and water (bottom). Reproduced with permission from ref. 144. Copyright 2016 Springer Nature.

surface was shielded by a hydrated Li^+-rich layer.[11] Both ionic layers push free water away from the electrode and extend the potential window to 3 V on stainless steel electrodes[144] (Fig. 10(e)).

With a WiSE (20 m LiTFSI), NCM622 delivered 152 mA h g^{-1} capacity for the first cycle and maintained its capacity for the 3rd cycle. This result was compared to the same electrode with 9 M LiNO$_3$, showing a 1st cycle capacity of 132 mA h g^{-1} and only ~79% capacity retention for the subsequent three cycles.[112] In addition, introducing additives to WiSE further stabilized LCO. Tris(trimethylsilyl) borate (TMSB) was sacrificially decomposed and formed a CEI layer.[122] With 21 m LiTFSI and 0.1 wt% TMSB, a 2.5 V-class of Mo$_6$S$_8$|LCO cells provided a 1st cycle capacity of 40 mA h g^{-1} at 2.5C after electrochemical activation, and the average capacity fading rate was 0.013% per cycle for 1000 cycles.

To mitigate water activity further, bisalts,[145] miscible non-aqueous solvents,[146] or ionic liquid was utilized.[121] LiTFSI was blended with LiBETI (BETI: N(SO$_2$C$_2$F$_5$)$_2$$^-$, bis(penta-fluoroethanesulfonyl)imide anion) to make Li(TFSI)$_{0.7}$(BETI)$_{0.3}$·2H$_2$O. It was a room-temperature hydrate-melt electrolyte, where the eutectic LiTFSI and LiBETI composition greatly limited water content.[123] A 2.4 V Li$_4$Ti$_5$O$_{12}$|LCO cell with Li(TFSI)$_{0.7}$(BETI)$_{0.3}$·2H$_2$O achieved 50 mA h g^{-1} capacity and 75% capacity retention after 200 cycles at 10C. A total 60 m electrolyte salt (40 m LiTFSI plus 20 m 1-ethyl-3-methylimidazolium TFSI (EMImTFSI)) attenuated Ni^{2+} dissolution and retarded capacity loss from NCM811, demonstrating better electrode stability than 21 m LiTFSI electrolyte.[147] However, the significant cost associated with the large quantities of electrolyte is a considerable burden, as it is currently more expensive than the non-aqueous electrolyte solution.

Artificial solid-state protective layers were implemented along with WiSE to inhibit electrode deterioration and limit electrolyte concentrations. A gel polymer electrolyte consisting of WiSE and UV curable polymer extended the cathodic limit to 1.41 V and the anodic limit to 4.86 V, leading to a 3.86 V potential window.[148] This approach was vital, in particular for the anode. Thus, graphite|LCO cells were first demonstrated using a gel electrolyte where 11 m LiTFSI in water and trimethylphosphate (TMP) was mixed with UV-curable monomers of poly(ethylene glycol) methyl ether acrylate (MPEGA), hydroxyethyl acrylate (HEA), and poly(ethylene glycol) diacrylate (PEGDA700), exhibiting a 3.8 V cell and 17 mA h capacity, which was 62% of the theoretical capacity.[149] Developing advanced artificial protective layers has mitigated a rapid cell failure, which has addressed challenges in aqueous LiBs effectively in conjunction with electrolyte engineering.

5. Conclusions and perspectives

LTMO demonstrated tunable properties in an aqueous electrolyte solution and extended its applications for the OER. There are three controlling factors: alkali-metal-ion vacancies, transition metal states, and oxygen lattices. Moderate formation of alkali-metal-ion vacancies increased the valence state of the transition metal in the oxide layer. If OER-active transition metals constituted LTMO, they became active sites for the OER with suitable valence states. Besides, O 2p band engineering activated the oxygen lattice of the oxide layer. Notably, when the oxygen lattice of LTMO participated in the OER, the activity was enhanced to a greater extent than with the activation of transition metals alone. However, the number of oxygen vacancies should be optimized to prevent severe oxide degradation. Further, introducing dopants improved OER activity, and nanostructuring the LTMO catalyst increased the surface area and enhanced the current density.

In addition to the above LTMO designs, we underlined that LTMO structures were often reconstructed during the OER due to the continuity of the deformed oxygen lattice and cation mixing. New crystalline or amorphous surfaces unexpectedly emerged and imposed strain and stress on LTMO. Various *in situ* X-ray and microscopy analytical tools were utilized to identify the reconstructed structures and address their OER activity linked with electrochemical evaluations. More importantly, even though the newly formed structure exhibited better OER activity, continuous structural transformation resulted in poor catalytic stability and reduced OER activity for long-term operation. For these reasons, the stability and consistency of the OER activity of LTMO have not yet become satisfactory for the practical level of water-splitting electrolyzers. Scrutinizing the time-dependent degradation mechanisms of LTMO and surface reconstruction trends associated with the above three controlling factors will help unveil the LTMO aging process. In this perspective, we showed several promising approaches to stabilize LTMO catalysts. The shallow insertion of Cs$^+$ into delithiated LCO negligibly changed the bulk LCO structure, while surface strains improved OER activity.[36] The cation electrolyte-mediated surface activation demonstrated improved catalytic stability compared to delithiated LCO. In another study, doping Cl$^-$ into LCO formed a new surface layer during the OER, which protected the bulk structure while performing OER activity.[34] These studies will guide the design of practical OER catalysts for H$_2$ production when considering electrochemical rebuilding processes.

On the other hand, investigations of LTMO cathodes for aqueous LiBs have been undertaken to enable cheap and grid-scale energy storage systems. However, vulnerability to water is a significant challenge for LTMO. Although the pH of the aqueous electrolyte solutions was selected at around 9 to avoid both the OER and H$^+$ attacks, H$^+$ permeation continued and led to electrode deformation and capacity fading in aqueous LiBs. To gain a better understanding of the interfacial reaction between LTMO and aqueous electrolyte solutions, various *in situ* and *ex situ* spectroscopic analyses have been conducted. These fundamental studies revealed that certain anions of the electrolyte, such as sulfate, chemically adsorbed onto LCO, acted as a barrier that prevented water and H$^+$ from accessing the electrode surface. A water-in-salt electrolyte was developed to form protective aggregated ion pair layers on LTMO cathodes and diminish the water activity, which eliminated the source of H$^+$. However, the insertion of water or H$^+$ into LTMO was not reasonably suppressed, particularly during slow charging and discharging processes and long-term cyclability. Their

performances were still inferior to non-aqueous LiBs, and the high cost of the massive amounts of electrolyte salts has not been resolved yet. Therefore, ground-breaking ideas are required for practical research approaches in aqueous LiBs.

We have exhibited the versatility of LTMO in two crucial applications in aqueous environments. We have gained a profound understanding of material properties through a wide range of approaches encompassing material designs, investigation of electrochemical processes, and evaluation of device performances. These efforts also highlighted key factors that need to be addressed to overcome the existing challenges. By leveraging the insights gained from these studies, we can drive forward the development of novel LTMO materials and technologies that will propel us toward a cleaner and more sustainable energy future.

Author contributions

Y. K., S. K., and E. C. wrote sessions 3, 2, and 4, respectively, under the direction of H. R. B., Y. K. and H. R. B. edited a whole manuscript.

Conflicts of interest

There are no conflicts to declare.

Acknowledgements

References

1 N. Dubouis and A. Grimaud, *Chem. Sci.*, 2019, **10**, 9165–9181.

2 X. Zou and Y. Zhang, *Chem. Soc. Rev.*, 2015, **44**, 5148–5180.

3 J. Song, C. Wei, Z. F. Huang, C. Liu, L. Zeng, X. Wang and Z. J. Xu, *Chem. Soc. Rev.*, 2020, **49**, 2196.

4 N. Zhang and Y. Chai, *Energy Environ. Sci.*, 2021, **14**, 4647–4671.

5 J. B. Goodenough and K. S. Park, *J. Am. Chem. Soc.*, 2013, **135**, 1167–1176.

6 M. Li, J. Lu, Z. Chen and K. Amine, *Adv. Mater.*, 2018, **30**, 1800561.

7 J. W. Fergus, *J. Power Sources*, 2010, **195**, 939–954.

8 A. Manthiram, *Nat. Commun.*, 2020, **11**, 1550.

9 C. M. Julien, A. Mauger, K. Zaghib and H. Groult, *Inorganics*, 2014, **2**, 132–154.

10 Z. I. Radzi, B. Vengadaesvaran, S. Ramesh and N. A. Rahim, in *Energy Materials*, ed. S. J. Dhoble, N. T. Kalyani, B. Vengadaesvaran and A. Kariem Arof, Elsevier, 2021, pp. 285–312.

11 C. Yang, J. Chen, T. Qing, X. Fan, W. Sun, A. Von Cresce, M. S. Ding, O. Borodin, J. Vatamanu, M. A. Schroeder, N. Eidson, C. Wang and K. Xu, *Joule*, 2017, **1**, 122–132.

12 Z. Lu, H. Wang, D. Kong, K. Yan, P.-C. Hsu, G. Zheng, H. Yao, Z. Liang, X. Sun and Y. Cui, *Nat. Commun.*, 2014, **5**, 4345.

13 S. Kobayashi, K. Nishio, M. Wilde, K. Fukutani, R. Shimizu and T. Hitosugi, *J. Phys. Chem. C*, 2023, **127**, 4684–4688.

14 W. T. Hong, K. A. Stoerzinger, Y.-L. Lee, L. Giordano, A. Grimaud, A. M. Johnson, J. Hwang, E. J. Crumlin, W. Yang and Y. Shao-Horn, *Energy Environ. Sci.*, 2017, **10**, 2190–2200.

15 Y. Li, X. Du, J. Huang, C. Wu, Y. Sun, G. Zou, C. Yang and J. Xiong, *Small*, 2019, **15**, e1901980.

16 H. Oh, H. Yamagishi, T. Ohta and H. R. Byon, *Mater. Chem. Front.*, 2021, **5**, 3657–3663.

17 H. Oh, S.-J. Shin, E. Choi, H. Yamagishi, T. Ohta, N. Yabuuchi, H.-G. Jung, H. Kim and H. R. Byon, *JACS Au*, 2023, **3**, 1392–1402.

18 J. Wandt, A. T. S. Freiberg, A. Ogrodnik and H. A. Gasteiger, *Mater. Today*, 2018, **21**, 825–833.

19 J. Hwang, S. Myeong, W. Jin, H. Jang, G. Nam, M. Yoon, S. H. Kim, S. H. Joo, S. K. Kwak, M. G. Kim and J. Cho, *Adv. Mater.*, 2020, **32**, 2001944.

20 T. Nagaura and K. Tozawa, *Prog. Batteries Sol. Cells*, 1990, **9**, 209–217.

21 M. A. Marquardt, N. A. Ashmore and D. P. Cann, *Thin Solid Films*, 2006, **496**, 146–156.

22 C. Delmas, C. Fouassier and P. Hagenmuller, *Physica B+C*, 1980, **99**, 81–85.

23 J. N. Reimers and J. R. Dahn, *J. Electrochem. Soc.*, 1992, **139**, 2091.

24 M. Okubo and A. Yamada, *ACS Appl. Mater. Interfaces*, 2017, **9**, 36463–36472.

25 T. Okumura, Y. Yamaguchi, M. Shikano and H. Kobayashi, *J. Mater. Chem.*, 2012, **22**, 17340–17348.

26 S.-K. Jung, H. Gwon, J. Hong, K.-Y. Park, D.-H. Seo, H. Kim, J. Hyun, W. Yang and K. Kang, *Adv. Energy Mater.*, 2014, **4**, 1300787.

27 P. Yan, L. Xiao, J. Zheng, Y. Zhou, Y. He, X. Zu, S. X. Mao, J. Xiao, F. Gao, J.-G. Zhang and C.-M. Wang, *Chem. Mater.*, 2015, **27**, 975–982.

28 R. Hausbrand, G. Cherkashinin, H. Ehrenberg, M. Gröting, K. Albe, C. Hess and W. Jaegermann, *Mater. Sci. Eng., B*, 2015, **192**, 3–25.

29 W. Liu, P. Oh, X. Liu, M.-J. Lee, W. Cho, S. Chae, Y. Kim and J. Cho, *Angew. Chem., Int. Ed. Engl.*, 2015, **54**, 4440–4457.

30 H. Sun and K. Zhao, *J. Phys. Chem. C*, 2017, **121**, 6002–6010.

31 J. Suntivich, K. J. May, H. A. Gasteiger, J. B. Goodenough and Y. Shao-Horn, *Science*, 2011, **334**, 1383–1385.

32 J. Hwang, R. R. Rao, L. Giordano, Y. Katayama, Y. Yu and Y. Shao-Horn, *Science*, 2017, **358**, 751–756.

33 H. Wang, J. Wu, A. Dolocan, Y. Li, X. Lu, N. Wu, K. Park, S. Xin, M. Lei, W. Yang and J. B. Goodenough, *Proc. Natl. Acad. Sci. U.S.A.*, 2019, **116**, 23473–23479.

34 J. Wang, S.-J. Kim, J. Liu, Y. Gao, S. Choi, J. Han, H. Shin, S. Jo, J. Kim, F. Ciucci, H. Kim, Q. Li, W. Yang, X. Long, S. Yang, S.-P. Cho, K. H. Chae, M. G. Kim, H. Kim and J. Lim, *Nat. Catal.*, 2021, **4**, 212–222.

35 S. Jiang, H. Suo, X. Zheng, T. Zhang, Y. Lei, Y. X. Wang, W. H. Lai and G. Wang, *Adv. Energy Mater.*, 2022, **12**, 2201934.

36 Y. Kim, S. Kim, M. Shim, Y. Oh, K.-S. Lee, Y. Jung and H. R. Byon, *J. Mater. Chem. A*, 2022, **10**, 10967–10978.

37 Y. Zhu, W. Zhou, Y. Chen, J. Yu, M. Liu and Z. Shao, *Adv. Mater.*, 2015, **27**, 7150–7155.

38 I. C. Man, H. Y. Su, F. Calle-Vallejo, H. A. Hansen, J. I. Martínez, N. G. Inoglu, J. Kitchin, T. F. Jaramillo, J. K. Nørskov and J. Rossmeisl, *ChemCatChem*, 2011, **3**, 1159–1165.

39 J. Bak, Y. Heo, T. G. Yun and S. Y. Chung, *ACS Nano*, 2020, **14**, 14323–14354.

40 J. R. Petrie, V. R. Cooper, J. W. Freeland, T. L. Meyer, Z. Zhang, D. A. Lutterman and H. N. Lee, *J. Am. Chem. Soc.*, 2016, **138**, 2488–2491.

41 Y. Heo, S. Choi, J. Bak, H.-S. Kim, H. B. Bae and S.-Y. Chung, *Adv. Energy Mater.*, 2018, **8**, 1802481.

42 M. J. Choi, T. L. Kim, J. K. Kim, T. H. Lee, S. A. Lee, C. Kim, K. Hong, C. W. Bark, K. T. Ko and H. W. Jang, *Nano Lett.*, 2020, **11**, 8040–8045.

43 R. Zhang, L. Pan, B. Guo, Z. F. Huang, Z. Chen, L. Wang, X. Zhang, Z. Guo, W. Xu, K. P. Loh and J. J. Zou, *J. Am. Chem. Soc.*, 2023, **145**, 2271–2281.

44 Y. Duan, S. Sun, Y. Sun, S. Xi, X. Chi, Q. Zhang, X. Ren, J. Wang, S. J. H. Ong, Y. Du, L. Gu, A. Grimaud and Z. J. Xu, *Adv. Mater.*, 2019, **31**, e1807898.

45 X. Rong, J. Parolin and A. M. Kolpak, *ACS Catal.*, 2016, **6**, 1153–1158.

46 A. Grimaud, O. Diaz-Morales, B. Han, W. T. Hong, Y. L. Lee, L. Giordano, K. A. Stoerzinger, M. T. M. Koper and Y. Shao-Horn, *Nat. Chem.*, 2017, **9**, 457–465.

47 Z. Zhang, C. Liu, C. Feng, P. Gao, Y. Liu, F. Ren, Y. Zhu, C. Cao, W. Yan, R. Si, S. Zhou and J. Zeng, *Nano Lett.*, 2019, **19**, 8774–8779.

48 J. T. Mefford, X. Rong, A. M. Abakumov, W. G. Hardin, S. Dai, A. M. Kolpak, K. P. Johnston and K. J. Stevenson, *Nat. Commun.*, 2016, **7**, 11053.

49 N. Zhang, X. Feng, D. Rao, X. Deng, L. Cai, B. Qiu, R. Long, Y. Xiong, Y. Lu and Y. Chai, *Nat. Commun.*, 2020, **11**, 4066.

50 Y. Pan, X. Xu, Y. Zhong, L. Ge, Y. Chen, J. M. Veder, D. Guan, R. O'Hayre, M. Li, G. Wang, H. Wang, W. Zhou and Z. Shao, *Nat. Commun.*, 2020, **11**, 2002.

51 C. Wei, Z. Feng, G. G. Scherer, J. Barber, Y. Shao-Horn and Z. J. Xu, *Adv. Mater.*, 2017, **29**, 1606800.

52 H. Li, S. Sun, S. Xi, Y. Chen, T. Wang, Y. Du, M. Sherburne, J. W. Ager, A. C. Fisher and Z. J. Xu, *Chem. Mater.*, 2018, **30**, 6839–6848.

53 J. Zhou, J. Li, L. Zhang, S. Song, Y. Wang, X. Lin, S. Gu, X. Wu, T.-C. Weng, J. Wang and S. Zhang, *J. Phys. Chem. C*, 2018, **122**, 14447–14458.

54 J. O. 'M. Bockris and T. Otagawa, *J. Electrochem. Soc.*, 1984, **131**, 290–302.

55 Y. Liu, H. Wang, D. Lin, C. Liu, P.-C. Hsu, W. Liu, W. Chen and Y. Cui, *Energy Environ. Sci.*, 2015, **8**, 1719–1724.

56 H. Y. Wang, S. F. Hung, H. Y. Chen, T. S. Chan, H. M. Chen and B. Liu, *J. Am. Chem. Soc.*, 2016, **138**, 36–39.

57 S. Zhang, S. Gu, Y. Wang, C. Liang, Y. Yu, L. Han, S. Zheng, N. Zhang, X. Liu, J. Zhou and J. Li, *ACS Catal.*, 2019, **9**, 7389–7397.

58 J. Gao, C. Q. Xu, S. F. Hung, W. Liu, W. Cai, Z. Zeng, C. Jia, H. M. Chen, H. Xiao, J. Li, Y. Huang and B. Liu, *J. Am. Chem. Soc.*, 2019, **141**, 3014–3023.

59 J. Zhou, L. Zhang, Y. C. Huang, C. L. Dong, H. J. Lin, C. T. Chen, L. H. Tjeng and Z. Hu, *Nat. Commun.*, 2020, **11**, 1984.

60 J. Timoshenko and B. Roldan Cuenya, *Chem. Rev.*, 2021, **121**, 882–961.

61 S. Song, Y. Wang, R. C. Davis, Z. Ren, X. Xiao, G. Yang, D. Wang, J. Bao, Q. Zhang, S. Chen and Z. Ren, *Chem. Mater.*, 2021, **33**, 6299–6310.

62 L. Sun, Z. Dai, L. Zhong, Y. Zhao, Y. Cheng, S. Chong, G. Chen, C. Yan, X. Zhang, H. Tan, L. Zhang, K. N. Dinh, S. Li, F. Ma and Q. Yan, *Appl. Catal., B*, 2021, **297**, 120477.

63 X. Li, W. Sun, C. Hao, Y. Bai, Z. Fu, Y. Lu, X. Wang and Z. Cheng, *J. Phys. Chem. Lett.*, 2022, **13**, 784–791.

64 X. Zheng, Y. Chen, X. Zheng, G. Zhao, K. Rui, P. Li, X. Xu, Z. Cheng, S. X. Dou and W. Sun, *Adv. Energy Mater.*, 2019, **9**, 1803482.

65 J. Dai, Y. Zhu, Y. Chen, W. Zhou and Z. Shao, *ACS Appl. Mater. Interfaces*, 2017, **9**, 21587–21592.

66 S. Chu, H. Sun, G. Chen, Y. Chen, W. Zhou and Z. Shao, *ACS Appl. Mater. Interfaces*, 2019, **11**, 25227–25235.

67 J. Wang, L. Li, H. Tian, Y. Zhang, X. Che and G. Li, *ACS Appl. Mater. Interfaces*, 2017, **9**, 7100–7107.

68 X. Zheng, Y. Chen, W. Lai, P. Li, C. Ye, N. Liu, S. X. Dou, H. Pan and W. Sun, *Adv. Funct. Mater.*, 2022, **32**, 2200663.

69 Z. Dai, Y. Liu, T. Liang, S. Lenus, Q. Liu, X. Zhang and P. Vijayakumar, *Appl. Mater. Today*, 2021, **25**, 2200663.

70 X. Zheng, P. Cui, Y. Qian, G. Zhao, X. Zheng, X. Xu, Z. Cheng, Y. Liu, S. X. Dou and W. Sun, *Angew Chem. Int. Ed. Engl.*, 2020, **59**, 14533–14540.

71 C. Yang, G. Rousse, K. Louise Svane, P. E. Pearce, A. M. Abakumov, M. Deschamps, G. Cibin, A. V. Chadwick, D. A. Dalla Corte, H. Anton Hansen, T. Vegge, J. M. Tarascon and A. Grimaud, *Nat. Commun.*, 2020, **11**, 1378.

72 A. Grimaud, K. J. May, C. E. Carlton, Y. L. Lee, M. Risch, W. T. Hong, J. Zhou and Y. Shao-Horn, *Nat. Commun.*, 2013, **4**, 2439.

73 T. Wang, Y. Sun, Y. Zhou, S. Sun, X. Hu, Y. Dai, S. Xi, Y. Du, Y. Yang and Z. J. Xu, *ACS Catal.*, 2018, **8**, 8568–8577.

74 J. Li, *Nano-Micro Lett.*, 2022, **14**, 112.

75 Y.-L. Lee, J. Kleis, J. Rossmeisl, Y. Shao-Horn and D. Morgan, *Energy Environ. Sci.*, 2011, **4**, 3966.

76 H. Ding, H. Liu, W. Chu, C. Wu and Y. Xie, *Chem. Rev.*, 2021, **121**, 13174–13212.

77 K. J. May, C. E. Carlton, K. A. Stoerzinger, M. Risch, J. Suntivich, Y.-L. Lee, A. Grimaud and Y. Shao-Horn, *J. Phys. Chem. Lett.*, 2012, **3**, 3264–3270.

78 Y. Zhou, S. Sun, J. Song, S. Xi, B. Chen, Y. Du, A. C. Fisher, F. Cheng, X. Wang, H. Zhang and Z. J. Xu, *Adv. Mater.*, 2018, **30**, 1802912.

79 D. A. Kuznetsov, B. Han, Y. Yu, R. R. Rao, J. Hwang, Y. Román-Leshkov and Y. Shao-Horn, *Joule*, 2018, **2**, 225–244.

80 J. Suntivich, W. T. Hong, Y.-L. Lee, J. M. Rondinelli, W. Yang, J. B. Goodenough, B. Dabrowski, J. W. Freeland and Y. Shao-Horn, *J. Phys. Chem. C*, 2014, **118**, 1856–1863.

81 Z. Xiao, Y. C. Huang, C. L. Dong, C. Xie, Z. Liu, S. Du, W. Chen, D. Yan, L. Tao, Z. Shu, G. Zhang, H. Duan, Y. Wang, Y. Zou, R. Chen and S. Wang, *J. Am. Chem. Soc.*, 2020, **142**, 12087–12095.

82 E. Marelli, J. Gazquez, E. Poghosyan, E. Muller, D. J. Gawryluk, E. Pomjakushina, D. Sheptyakov, C. Piamonteze, D. Aegerter, T. J. Schmidt, M. Medarde and E. Fabbri, *Angew Chem. Int. Ed. Engl.*, 2021, **60**, 14609–14619.

83 R. Zhang, Y.-C. Zhang, L. Pan, G.-Q. Shen, N. Mahmood, Y.-H. Ma, Y. Shi, W. Jia, L. Wang, X. Zhang, W. Xu and J.-J. Zou, *ACS Catal.*, 2018, **8**, 3803–3811.

84 J.-W. Zhao, H. Zhang, C.-F. Li, X. Zhou, J.-Q. Wu, F. Zeng, J. Zhang and G.-R. Li, *Energy Environ. Sci.*, 2022, **15**, 3912–3922.

85 B. Liu, Y. Wang, H. Q. Peng, R. Yang, Z. Jiang, X. Zhou, C. S. Lee, H. Zhao and W. Zhang, *Adv. Mater.*, 2018, **30**, 1803144.

86 X. Miao, L. Wu, Y. Lin, X. Yuan, J. Zhao, W. Yan, S. Zhou and L. Shi, *Chem. Commun.*, 2019, **55**, 1442–1445.

87 S.-H. Hsu, S.-F. Hung, H.-Y. Wang, F.-X. Xiao, L. Zhang, H. Yang, H. M. Chen, J.-M. Lee and B. Liu, *Small Methods*, 2018, **2**, 1800001.

88 H. Liu, J. Qi, H. Xu, J. Li, F. Wang, Y. Zhang, M. Feng and W. Lü, *ACS Catal.*, 2022, **12**, 4119–4124.

89 S. W. Lee, C. Carlton, M. Risch, Y. Surendranath, S. Chen, S. Furutsuki, A. Yamada, D. G. Nocera and Y. Shao-Horn, *J. Am. Chem. Soc.*, 2012, **134**, 16959–16962.

90 B. Han, D. Qian, M. Risch, H. Chen, M. Chi, Y. S. Meng and Y. Shao-Horn, *J. Phys. Chem. Lett.*, 2015, **6**, 1357–1362.

91 N. Colligan, V. Augustyn and A. Manthiram, *J. Phys. Chem. C*, 2015, **119**, 2335–2340.

92 Z. Lu, G. Chen, Y. Li, H. Wang, J. Xie, L. Liao, C. Liu, Y. Liu, T. Wu, Y. Li, A. C. Luntz, M. Bajdich and Y. Cui, *J. Am. Chem. Soc.*, 2017, **139**, 6270–6276.

93 T. G. Yun, Y. Heo, H. Bin Bae and S. Y. Chung, *Nat. Commun.*, 2021, **12**, 824.

94 J. I. Jung, H. Y. Jeong, J. S. Lee, M. G. Kim and J. Cho, *Angew Chem. Int. Ed. Engl.*, 2014, **53**, 4582–4586.

95 J. Bak, H. Bin Bae and S. Y. Chung, *Nat. Commun.*, 2019, **10**, 2713.

96 A. Gupta, W. D. Chemelewski, C. Buddie Mullins and J. B. Goodenough, *Adv. Mater.*, 2015, **27**, 6063–6067.

97 X. Li, Q. Wang, H. Guo, N. Artrith and A. Urban, *ACS Appl. Energy Mater.*, 2022, **5**, 5730–5741.

98 D. Y. Chung, P. P. Lopes, P. Farinazzo Bergamo Dias Martins, H. He, T. Kawaguchi, P. Zapol, H. You, D. Tripkovic, D. Strmcnik, Y. Zhu, S. Seifert, S. Lee, V. R. Stamenkovic and N. M. Markovic, *Nat. Energy*, 2020, **5**, 222–230.

99 P. P. Lopes, D. Y. Chung, X. Rui, H. Zheng, H. He, P. Farinazzo Bergamo Dias Martins, D. Strmcnik, V. R. Stamenkovic, P. Zapol, J. F. Mitchell, R. F. Klie and N. M. Markovic, *J. Am. Chem. Soc.*, 2021, **143**, 2741–2750.

100 M. S. Burke, M. G. Kast, L. Trotochaud, A. M. Smith and S. W. Boettcher, *J. Am. Chem. Soc.*, 2015, **137**, 3638–3648.

101 J. Bak, T. G. Yun, J.-S. An, H. B. Bae and S.-Y. Chung, *Energy Environ. Sci.*, 2022, **15**, 610–620.

102 Y. Wang, J. Ren, Y. Wang, F. Zhang, X. Liu, Y. Guo and G. Lu, *J. Phys. Chem. C*, 2008, **112**, 15293–15298.

103 F. Liang, Y. Yu, W. Zhou, X. Xu and Z. Zhu, *J. Mater. Chem. A*, 2015, **3**, 634–640.

104 G. Cheng, T. Kou, J. Zhang, C. Si, H. Gao and Z. Zhang, *Nano Energy*, 2017, **38**, 155–166.

105 L. Bai, C. S. Hsu, D. T. L. Alexander, H. M. Chen and X. Hu, *J. Am. Chem. Soc.*, 2019, **141**, 14190–14199.

106 Y. Miyahara, T. Fukutsuka, T. Abe and K. Miyazaki, *Chem. Mater.*, 2020, **32**, 8195–8202.

107 L. Gui, Y. Liu, J. Zhang, B. He, Q. Wang and L. Zhao, *J. Mater. Chem. A*, 2020, **8**, 19946–19953.

108 T. Wu, S. Sun, J. Song, S. Xi, Y. Du, B. Chen, W. A. Sasangka, H. Liao, C. L. Gan, G. G. Scherer, L. Zeng, H. Wang, H. Li, A. Grimaud and Z. J. Xu, *Nat. Catal.*, 2019, **2**, 763–772.

109 Q. Cheng, T. Yang, Y. Li, M. Li and C. K. Chan, *J. Mater. Chem. A*, 2016, **4**, 6902–6910.

110 R. Ruffo, C. Wessells, R. A. Huggins and Y. Cui, *Electrochem. Commun.*, 2009, **11**, 247–249.

111 R. Ruffo, F. La Mantia, C. Wessells, R. A. Huggins and Y. Cui, *Solid State Ionics*, 2011, **192**, 289–292.

112 M. Kunduraci, R. N. Mutlu and A. M. Gizir, *Ionics*, 2020, **26**, 1663–1672.

113 W. Tang, L. L. Liu, S. Tian, L. Li, Y. B. Yue, Y. P. Wu, S. Y. Guan and K. Zhu, *Electrochem. Commun.*, 2010, **12**, 1524–1526.

114 G. Wang, L. Fu, N. Zhao, L. Yang, Y. Wu and H. Wu, *Angew. Chem., Int. Ed. Engl.*, 2007, **46**, 295–297.

115 G. J. Wang, N. H. Zhao, L. C. Yang, Y. P. Wu, H. Q. Wu and R. Holze, *Electrochim. Acta*, 2007, **52**, 4911–4915.

116 X. Wang, Q. Qu, Y. Hou, F. Wang and Y. Wu, *Chem. Commun.*, 2013, **49**, 6179–6181.

117 J. Köhler, H. Makihara, H. Uegaito, H. Inoue and M. Toki, *Electrochim. Acta*, 2000, **46**, 59–65.

118 G. J. Wang, L. J. Fu, B. Wang, N. H. Zhao, Y. P. Wu and R. Holze, *J. Appl. Electrochem.*, 2008, **38**, 579–581.

119 L. Liu, F. Tian, X. Wang, Z. Yang, Q. Chen and X. Wang, *J. Solid State Electrochem.*, 2012, **16**, 491–497.

120 R. B. Shivashankaraiah, H. Manjunatha, K. C. Mahesh, G. S. Suresh and T. V. Venkatesha, *J. Solid State Electrochem.*, 2012, **16**, 1279–1290.

121 M. Becker, D. Rentsch, D. Reber, A. Aribia, C. Battaglia and R. S. Kühnel, *Angew. Chem., Int. Ed. Engl.*, 2021, **60**, 14100–14108.

122 F. Wang, Y. Lin, L. Suo, X. Fan, T. Gao, C. Yang, F. Han, Y. Qi, K. Xu and C. Wang, *Energy Environ. Sci.*, 2016, **9**, 3666–3673.

123 Y. Yamada, K. Usui, K. Sodeyama, S. Ko, Y. Tateyama and A. Yamada, *Nat. Energy*, 2016, **1**, 16129.

124 J. Qian, L. Liu, J. Yang, S. Li, X. Wang, H. L. Zhuang and Y. Lu, *Nat. Commun.*, 2018, **9**, 4918.

125 L. Noerochim, S. Suwarno, N. H. Idris and H. K. Dipojono, *Batteries*, 2021, **7**, 84.

126 C. Lee, Y. Miyahara, T. Abe and K. Miyazaki, *J. Power Sources*, 2022, **524**, 231081.

127 S. S. Zhang, J. Chen and C. Wang, *J. Electrochem. Soc.*, 2019, **166**, A487–A492.

128 W. Li, J. R. Dahn and D. S. Wainwright, *Science*, 1994, **264**, 1115–1118.

129 I. A. Shkrob, J. A. Gilbert, P. J. Phillips, R. Klie, R. T. Haasch, J. Bareño and D. P. Abraham, *J. Electrochem. Soc.*, 2017, **164**, A1489–A1498.

130 R. Benedek, M. M. Thackeray and A. Van De Walle, *Chem. Mater.*, 2008, **20**, 5485–5490.

131 J. Choi, E. Alvarez, T. A. Arunkumar and A. Manthiram, *Electrochem. Solid-State Lett.*, 2006, **9**, A241.

132 X. Gu, J.-L. Liu, J.-H. Yang, H.-J. Xiang, X.-G. Gong and Y.-Y. Xia, *J. Phys. Chem. C*, 2011, **115**, 12672–12676.

133 S. Posada-Pérez, G.-M. Rignanese and G. Hautier, *Chem. Mater.*, 2021, **33**, 6942–6954.

134 A. Ramanujapuram, D. Gordon, A. Magasinski, B. Ward, N. Nitta, C. Huang and G. Yushin, *Energy Environ. Sci.*, 2016, **9**, 1841–1848.

135 H. J. Lee, J. H. Lee, I. H. Son, S. Han, P. Byeon, M.-S. Park, S.-Y. Chung and J. W. Choi, *ACS Appl. Energy Mater.*, 2018, **1**, 5726–5734.

136 L. Suo, O. Borodin, T. Gao, M. Olguin, J. Ho, X. Fan, C. Luo, C. Wang and K. Xu, *Science*, 2015, **350**, 938–943.

137 J. Lim, K. Park, H. Lee, J. Kim, K. Kwak and M. Cho, *J. Am. Chem. Soc.*, 2018, **140**, 15661–15667.

138 O. Borodin, L. Suo, M. Gobet, X. Ren, F. Wang, A. Faraone, J. Peng, M. Olguin, M. Schroeder, M. S. Ding, E. Gobrogge, A. von Wald Cresce, S. Munoz, J. A. Dura, S. Greenbaum, C. Wang and K. Xu, *ACS Nano*, 2017, **11**, 10462–10471.

139 X. Liu, S.-C. Lee, S. Seifert, L. He, C. Do, R. E. Winans, G. Kwon, Y. Zhang and T. Li, *Chem. Mater.*, 2023, **35**, 2088–2094.

140 J. Kim, B. Koo, J. Lim, J. Jeon, C. Lim, H. Lee, K. Kwak and M. Cho, *ACS Energy Lett.*, 2022, **7**, 189–196.

141 R. Zhang, M. Han, K. Ta, K. E. Madsen, X. Chen, X. Zhang, R. M. Espinosa-Marzal and A. A. Gewirth, *ACS Appl. Energy Mater.*, 2020, **3**, 8086–8094.

142 M. McEldrew, Z. A. H. Goodwin, A. A. Kornyshev and M. Z. Bazant, *J. Phys. Chem. Lett.*, 2018, **9**, 5840–5846.

143 M. Han, R. Zhang, A. A. Gewirth and R. M. Espinosa-Marzal, *Nano Lett.*, 2021, **21**, 2304–2309.

144 K. Xu and C. Wang, *Nat. Energy*, 2016, **1**, 16161.

145 L. Suo, O. Borodin, W. Sun, X. Fan, C. Yang, F. Wang, T. Gao, Z. Ma, M. Schroeder, A. Von Cresce, S. M. Russell, M. Armand, A. Angell, K. Xu and C. Wang, *Angew. Chem., Int. Ed. Engl.*, 2016, **55**, 7136–7141.

146 Y. Huang, W. Sun, K. Xu, J. Zhang, H. Zhang, J. Li, L. He, L. Cai, F. Fu, J. Qin and H. Chen, *Energy Storage Mater.*, 2022, **46**, 577–582.

147 M. Becker, W. Zhao, F. Pagani, C. Schreiner, R. Figi, W. Dachraoui, R. Grissa, R.-S. Kühnel and C. Battaglia, *ACS Appl. Energy Mater.*, 2022, **5**, 11133–11141.

148 J. Zhang, C. Cui, P.-F. Wang, Q. Li, L. Chen, F. Han, T. Jin, S. Liu, H. Choudhary, S. R. Raghavan, N. Eidson, A. Von Cresce, L. Ma, J. Uddin, D. Addison, C. Yang and C. Wang, *Energy Environ. Sci.*, 2020, **13**, 2878–2887.

149 A. Cresce, N. Eidson, M. Schroeder, L. Ma, Y. Howarth, C. Yang, J. Ho, R. Dillon, M. Ding, A. Bassett, J. Stanzione, R. Tom, T. Soundappan, C. Wang and K. Xu, *J. Power Sources*, 2020, **469**, 228378.